

Hemodynamic Deconvolution Demystified: Sparsity-Driven Regularization at Work

Eneko Uruñuela^{a,b,*}, Thomas A.W. Bolton^{c,d}, Dimitri Van De Ville^{d,e}, César Caballero-Gaudes^a

^a*Basque Center on Cognition, Brain and Language (BCBL), Donostia-San Sebastián, Spain.*

^b*University of the Basque Country (EHU/UPV), Donostia-San Sebastián, Spain.*

^c*Gamma Knife Center, Department of Clinical Neuroscience, Centre Hospitalier Universitaire Vaudois (CHUV), Lausanne, Switzerland*

^d*Ecole Polytechnique Fédérale de Lausanne (EPFL), Lausanne, Switzerland.*

^e*Faculty of Medicine, University of Geneva, Geneva, Switzerland*

Abstract

Deconvolution of the hemodynamic response is an important step to access short timescales of brain activity recorded by functional magnetic resonance imaging (fMRI). Albeit conventional deconvolution algorithms have been around for a long time (e.g., Wiener deconvolution), recent state-of-the-art methods based on sparsity-pursuing regularization are attracting increasing interest to investigate brain dynamics and connectivity. This technical note revisits the main concepts underlying two main methods, Paradigm Free Mapping and Total Activation, in the most accessible way. Despite their apparent differences, these methods are theoretically equivalent as they represent the synthesis and analysis sides of the same problem. We demonstrate this equivalence in practice with their best-available implementations using both simulations, with different signal-to-noise ratios, and experimental data of motor task and resting-state fMRI. We evaluate the parameter settings that lead to equivalent results, and showcase the potential of these algorithms compared to other widely-used approaches. This note is useful for practitioners interested in having a better understanding of state-of-the-art hemodynamic deconvolution, and who want to make use of them in the most efficient implementation.

Keywords: fMRI deconvolution, paradigm free mapping, total activation, temporal regularization

1. Introduction

Functional magnetic resonance imaging (fMRI) data analysis is often directed to identify and disentangle the neural processes that occur in different brain regions during task or at rest. As the blood oxygenation level-dependent (BOLD) signal of fMRI is only a proxy for neuronal activity mediated through neurovascular coupling, an intermediate step that estimates the activity-inducing signal, at the timescale of fMRI, from the BOLD timeseries can be useful. Conventional analysis of task fMRI data relies on the general linear models (GLM) to establish statistical parametric maps of brain activity by regression of the empirical timecourses against hypothetical ones built from

*Corresponding author

Email address: e.urunuela@bcbl.eu (Eneko Uruñuela)

the knowledge of the experimental paradigm. However, timing information of the paradigm can be
10 unknown, inaccurate, or insufficient in some scenarios such as naturalistic stimuli, resting-state, or
clinically-relevant assessments.

Deconvolution and methods alike are aiming to estimate neuronal activity by undoing the blurring effect of the hemodynamic response, characterized as a hemodynamic response function (HRF). Given the inherently ill-posed nature of hemodynamic deconvolution, due to the strong temporal
15 low-pass characteristics of the HRF, the key is to introduce additional constraints in the estimation problem that are typically expressed as regularizers. For instance, the so-called Wiener deconvolution is expressing a “minimal energy” constraint on the deconvolved signal, and has been used in the framework of psychophysiological interactions analysis to compute the interaction between a seed’s activity-inducing timecourse and an experimental modulation (Glover 1999; Gitelman et al.
20 2003; Gerchen et al. 2014; Di and Biswal 2018; Freitas et al. 2020). Complementarily, the interest in deconvolution has increased to explore time-varying activity in resting-state fMRI data (Prete et al. 2017; Keilholz et al. 2017; Lurie et al. 2020; Bolton et al. 2020). In that case, the aim is to gain better insights into the neural signals that drive functional connectivity at short time scales, as well as how the spatio-temporal structure of functional components that dynamically construct
25 resting-state networks and their interactions (Karahanoglu and Ville 2017).

Deconvolution of the resting-state fMRI signal has illustrated the significance of transient, sparse spontaneous events (Petridou et al. 2012; Allan et al. 2015) that refine the hierarchical clusterization of functional networks (Karahanoglu et al. 2013) and reveal their temporal overlap based on their signal innovations not only in the human brain (Karahanoglu and Ville 2015), but also in the spinal cord (Kinany et al. 2020). Similar to task-related studies, deconvolution allows to investigate modulatory interactions within and between resting-state functional networks (Di and Biswal 2013, 2015). In addition, decoding of the deconvolved spontaneous events allows to decipher the flow of spontaneous thoughts and actions across different cognitive and sensory domains while at rest (Karahanoglu and Ville 2015; Gonzalez-Castillo et al. 2019; ?). Beyond findings on healthy subjects,
30 35 deconvolution techniques has also proven its utility in clinical conditions to characterize functional alterations of patients with a progressive stage of multiple sclerosis at rest (Bommarito et al. 2020), to find functional signatures of prodromal psychotic symptoms and anxiety at rest on patients suffering from schizophrenia (Zöller et al. 2019), to detect the foci of interictal events in epilepsy patients without an EEG recording (Lopes et al. 2012; Karahanoglu et al. 2013), or to study functional dissociations observed during non-rapid eye movement sleep that are associated with reduced consolidation of information and impaired consciousness (Tarun et al. 2020).

The algorithms for hemodynamic deconvolution can be classified based on the assumed hemodynamic model and the optimization problem used to estimate the neuronal-related signal. Most approaches assume a linear time-invariant model for the hemodynamic response that is inverted
45 by means of variational (regularized) least squares estimators (Glover 1999; Gitelman et al. 2003; Gaudes et al. 2010, 2012, 2013; Caballero-Gaudes et al. 2019; Hernandez-Garcia and Ulfarsson 2011; Karahanoglu et al. 2013; Cherkaoui et al. 2019; Costantini et al. 2021; Hütel et al. 2021), logistic functions (Bush and Cisler 2013; Bush et al. 2015; Loula et al. 2018), probabilistic mixture models (Pidnebesna et al. 2019), convolutional autoencoders (Hütel et al. 2018) or nonparametric homomorphic filtering (Sreenivasan et al. 2015). Alternatively, several methods have also been proposed to invert non-linear models of the neuronal and hemodynamic coupling (Riera et al. 2004; Friston et al. 2008; Havlicek et al. 2011; Aslan et al. 2016; Madi and Karameh 2017; Ruiz-Euler et al. 2018).

Among the variety of approaches, those based on regularized least squares estimators have been employed more often due to their appropriate performance at small spatial scales (e.g. voxelwise).

55 Relevant for this work, two different formulations can be established for the regularized least squares problem, either based on a synthesis-based or analysis-based model (Elad et al. 2007; Ortelli and van de Geer 2019). The rationale of the synthesis-based model is that we know or suspect that the true signal (here, the neuronally-driven BOLD component of the fMRI signal) can be represented as a linear combination of predefined patterns or dictionary atoms (for instance, the hemodynamic response function). In contrast, the analysis-based approach considers that the true signal is analyzed by some relevant operator and the resulting signal is small (i.e. sparse).

60 This note revisits synthesis- and analysis-based deconvolution methods for fMRI data and comprises four sections. In the first, we present the theory behind two state-of-the-art deconvolution approaches based on regularized least squares estimators that promote sparsity: Paradigm Free
65 Mapping (PFM) (Gaudes et al. 2013) — available in AFNI as *3dPFM* and *3dMEPFM* for single-echo and multi-echo data, respectively — and Total Activation (TA) (Karahanoglu et al. 2013) — available as part of the *iCAPs toolbox*. We then assess their performance controlling for a fair comparison on simulated and experimental data. Finally, we discuss the benefits and shortcomings of each technique and conclude with our vision on potential extensions and developments.

70 2. Theory

2.1. Notations and definitions

Matrices of size N rows and M columns are denoted by boldface capital letters, e.g., $\mathbf{X} \in \mathcal{R}^{N \times M}$, whereas column vectors of length N are denoted as boldface lowercase letters, e.g. $\mathbf{x} \in \mathcal{R}^N$. Scalars are denoted by lowercase letters, e.g., k . Continuous functions are denoted by brackets, e.g., $h(t)$, while discrete functions are denoted by square brackets, e.g., $x[k]$. The euclidean norm of a matrix \mathbf{X} is denoted as $\|\mathbf{X}\|_2$, the ℓ_1 -norm is denoted by $\|\mathbf{X}\|_1$ and the Frobenius norm is denoted by $\|\mathbf{X}\|_F$.

2.2. Conventional general linear model analysis

Conventional general linear model (GLM) analysis puts forward a number of regressors incorporating hypothetical knowledge about the paradigm or behavior. For instance, the timing of epochs for a certain condition can be modeled as an indicator function $p(t)$ (e.g. Dirac functions for event-related designs or box-car functions for block-designs) convolved with the hemodynamic response function (HRF) $h(t)$, and sampled at TR resolution (Friston et al. 1994, 1998; Boynton et al. 1996; Cohen 1997):

$$p(t) \rightarrow p * h(t) \rightarrow x[k] = p * h(k \cdot \text{TR}).$$

The vector $\mathbf{x} = [x[k]]_{k=1,\dots,N} \in \mathcal{R}^N$ then constitutes the regressor modelling the hypothetical response, and several of them can be stacked as columns of the design matrix $\mathbf{X} = [\mathbf{x}_1 \dots \mathbf{x}_L] \in \mathcal{R}^{N \times L}$, leading to the well-known GLM formulation:

$$\mathbf{y} = \mathbf{X}\boldsymbol{\beta} + \mathbf{e}, \quad (1)$$

where the empirical timecourse $\mathbf{y} \in \mathcal{R}^N$ is explained by a linear combination of the regressors in \mathbf{X} weighted by the parameters in $\boldsymbol{\beta} \in \mathcal{R}^L$ and corrupted by additive noise $\mathbf{e} \in \mathcal{R}^N$. Under independent and identically distributed Gaussian assumptions of the latter, the maximum likelihood estimate of the parameter weights reverts to the ordinary least-squares estimator; i.e., minimizing the residual sum of squares between the fitted model and measurements. The number of regressors L is typically

much less than the number of measurements N , and thus the regression problem is over-determined
⁸⁵ and does no require additional constraints or assumptions.

In the deconvolution approach, no prior knowledge of the hypothetical response is taken into account, and the purpose is to estimate the deconvolved activity-inducing signal \mathbf{s} from the measurements \mathbf{y} , which can be formulated as the signal model

$$\mathbf{y} = \mathbf{H}\mathbf{s} + \mathbf{e}, \quad (2)$$

where $\mathbf{H} \in \mathcal{R}^{N \times N}$ is a Toeplitz matrix that represents the discrete convolution with the HRF, and $\mathbf{s} \in \mathcal{R}^N$ is a length- N vector with the unknown activity-inducing signal. Note that the temporal resolution of the activiy-inducing signal and the corresponding Toeplitz matrix is generally assumed to be equal to TR of the acquisition, but it could also be higher if an upsampled estimate is desired. Despite the apparent similarity with the GLM equation, there are two important differences. First, the multiplication with the design matrix of the GLM is an expansion as a weighted linear combination of its columns, while the multiplication with the HRF matrix represents a convolution operator. Second, determining \mathbf{s} is an ill-posed problem given the nature of the HRF. As it can be seen intuitively, the convolution matrix \mathbf{H} is highly collinear (i.e. its columns are highly correlated) due to large overlap between shifted HRFs (see Figure 2C), thus introducing large variability in the estimates of \mathbf{s} . Consequently, additional assumptions under the form of regularization terms (or priors) in the estimate are needed to reduce their variance. In the least squares sense, the optimization problem to solve is given by

$$\hat{\mathbf{s}} = \arg \min_{\mathbf{s}} \frac{1}{2} \|\mathbf{y} - \mathbf{H}\mathbf{s}\|_2^2 + \Omega(\mathbf{s}). \quad (3)$$

The first term quantifies data fitness, which can be justified as the log-likelihood term derived from Gaussian noise assumptions, while the second term $\Omega(\mathbf{s})$ brings in regularization and be interpreted as a prior on the activity-inducing signal. For example, the ℓ_2 -norm of \mathbf{s} (i.e., $\Omega(\mathbf{s}) = \lambda \|\mathbf{s}\|_2^2$) is imposed for ridge regression or Wiener deconvolution, which introduces a trade-off between the data fit term and “energy” of the estimates that is controlled by the regularization parameter λ .
⁹⁰

2.3. Paradigm free mapping

In paradigm free mapping (PFM), the formulation of Eq. (3) was considered equivalently as fitting the measurements using the atoms of the HRF dictionary (i.e. columns of \mathbf{H}) with corresponding weights (entries of \mathbf{s}). This model corresponds to a synthesis formulation. In Gaudes et al. 2013 a sparsity-pursuing regularization term was introduced on \mathbf{s} , which in a strict way reverts to choosing $\Omega(\mathbf{s}) = \lambda \|\mathbf{s}\|_0$ as the regularization term and solving the optimization problem (Bruckstein et al. 2009). However, finding the optimal solution to the problem demands an exhaustive search across all possible combinations of the columns of \mathbf{H} . Hence, a pragmatic solution is to solve the convex-relaxed optimization problem for the ℓ_1 -norm, commonly known as Basis Pursuit Denoising (Chen et al. 2001) or equivalently as the least absolute shrinkage and selection operator (LASSO) (Tibshirani 1996):

$$\hat{\mathbf{s}} = \arg \min_{\mathbf{s}} \frac{1}{2} \|\mathbf{y} - \mathbf{H}\mathbf{s}\|_2^2 + \lambda \|\mathbf{s}\|_1, \quad (4)$$

which provides fast convergence to a global solution. Imposing sparsity on the activity-inducing signal implies that it is assumed to be well represented by a reduced subset of few non-zero coefficients at the fMRI timescale, which in turn trigger event-related BOLD responses. Hereinafter, we refer to this assumption as the spike model.
⁹⁵

2.4. Total activation

Alternatively, deconvolution can be formulated as if the signal to be recovered directly fits the measurements and at the same time satisfies some suitable regularization, which leads to

$$\hat{\mathbf{x}} = \arg \min_{\mathbf{x}} \frac{1}{2} \|\mathbf{y} - \mathbf{x}\|_2^2 + \Omega(\mathbf{x}). \quad (5)$$

Under this analysis formulation, total variation (TV), i.e. the ℓ_1 -norm of the derivative $\Omega(\mathbf{x}) = \lambda \|\mathbf{Dx}\|_1$, is a powerful regularizer since it favors recovery of piecewise-constant signals (Chambolle 2004). Going beyond, the approach of generalized TV introduces an additional differential operator \mathbf{D}_H in the regularizer that can be tailored as the inverse operator of a linear system (Karananoglu et al. 2011), that is, $\Omega(\mathbf{x}) = \lambda \|\mathbf{DD}_H\mathbf{x}\|_1$. In the context of hemodynamic deconvolution, total activation is proposed for which the discrete operator \mathbf{D}_H is derived from the inverse of the continuous-domain linearized Balloon-Windkessel model (Buxton et al. 1998; Friston et al. 2000). Exchanging the poles and zeros of the latter's linear-system characterization leads to a differential operator of the form

$$D_H = \prod_{i=1}^{M_1} (D - \alpha_i I) \left(\prod_{j=1}^{M_2} (D - \gamma_j I) \right)^{-1}, \quad (6)$$

where D is the derivative operator, α_i the zeros, and γ_j the poles. The interested reader is referred to (Khalidov et al. 2011; Karahanoglu et al. 2011; Karahanoğlu et al. 2013) for a detailed description.

Therefore, the solution of the total activation (TA) problem

$$\hat{\mathbf{x}} = \arg \min_{\mathbf{x}} \frac{1}{2} \|\mathbf{y} - \mathbf{x}\|_2^2 + \lambda \|\mathbf{DD}_H\mathbf{x}\|_1 \quad (7)$$

will render the activity-related signal \mathbf{x} for which the activity-inducing signal $\mathbf{s} = \mathbf{D}_H\mathbf{x}$ and the so-called innovation signal $\mathbf{u} = \mathbf{Ds}$ will also be available, as they are required for the regularization. We refer to modelling the activity-inducing signal based on the innovation signal as the block model.

2.5. Unifying both perspectives

PFM and TA are based on the synthesis- and analysis-based formulation of the deconvolution problem, respectively. In the first case, the recovered deconvolved signal is synthesized to be matched to the measurements, while in the second case, the recovered signal is directly matched to the measurements but needs to satisfy its analysis in terms of deconvolution. This also corresponds to using the forward or backward model of the hemodynamic system, respectively. Hence, it should be possible to make both approaches equivalent (Elad et al. 2007)¹.

First, TA can be made equivalent to PFM by removing the derivative operator \mathbf{D} of the regularizer in Eq. (7). It can then be readily verified that replacing in that case $\mathbf{x} = \mathbf{Hs}$ leads to identical equations and thus both assume a spike model.

Second, the PFM optimization problem in Eq. (4) can also be made equivalent to the TA block model in Eq. (7) by considering the modified forward model $\mathbf{y} = \mathbf{HLu} + \mathbf{e}$. Here, the activity-inducing signal \mathbf{s} is rewritten in terms of the innovation signal \mathbf{u} as $\mathbf{s} = \mathbf{Lu}$ where the matrix \mathbf{L} is

I would exclude this part of Equation 6, and refer to the paper of activelets and TA for more information

Do you think it's necessary to include the explicit relationship between the matrices \mathbf{H} and \mathbf{D}_H , and also write down \mathbf{D} and \mathbf{L} analytically?

¹Without dwelling into technicalities, this equivalence is correct up to the constant, which is in the null space of the derivative operator.

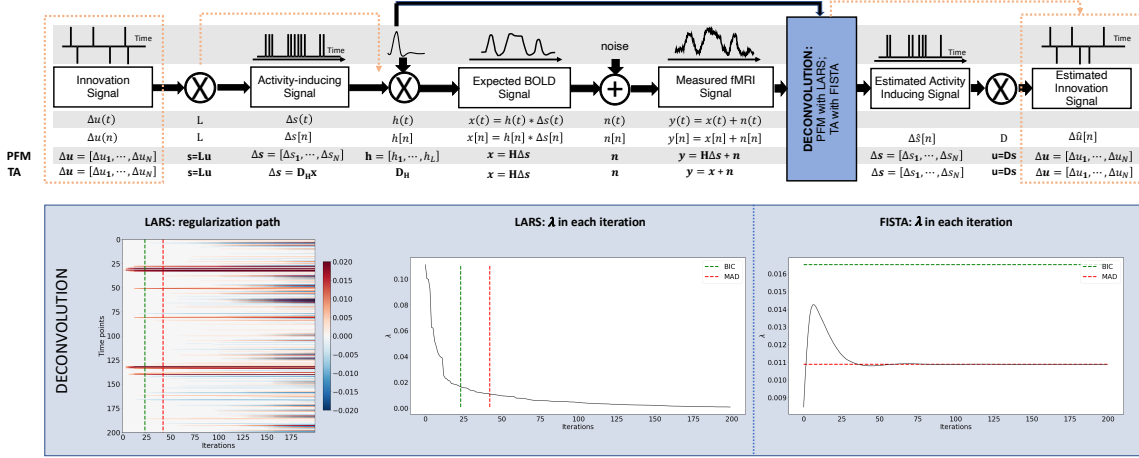


Figure 1: Flowchart detailing the different steps of the fMRI signal and the deconvolution methods described. The orange arrows indicate the flow to estimate the innovation signals. The blue box depicts the operations involved in two algorithms used in this paper to solve the PFM and TA deconvolution problems. The left plot shows the regularization path obtained with LARS, where the x-axis illustrates the different iterations of the algorithm, the y-axis represents points in time, and the color describes the amplitude of the estimated signal. The middle plot depicts the decreasing values of λ for each iteration of LARS as the regularization path is computed. The green and red dashed lines in both plots illustrate the BIC and MAD solutions, respectively. Comparatively, the changes in λ when the FISTA method is made to converge to the MAD estimate of the noise are shown on the right. Likewise, the λ corresponding to the BIC and MAD solutions are shown with dashed lines.

the first-order integration operator (Cherkaoui et al. 2019; Uruñuela et al. 2020). This way, PFM can also estimate the innovation signal \mathbf{u} as follows:

$$\hat{\mathbf{u}} = \arg \min_{\mathbf{u}} \frac{1}{2} \|\mathbf{y} - \mathbf{H}\mathbf{L}\mathbf{u}\|_2^2 + \lambda \|\mathbf{u}\|_1, \quad (8)$$

and becomes equivalent to TA by replacing $\mathbf{u} = \mathbf{D}\mathbf{D}_H\mathbf{x}$, and thus adopting the block model.

This work evaluates the core of the two techniques, i.e., the regularized least-squares problem with temporal regularization. Therefore, we do not study the impact of spatial constraints, as we assume that spatial regularization terms should perform identically on both methods.

2.6. Algorithms and parameter selection

Despite their analytical equivalence, the PFM and TA methods proposed different different strategies to solve the corresponding optimization problem and select an adequate regularization parameter λ . The PFM implementation available in AFNI employs the least angle regression (LARS) (Efron et al. 2004), whereas the TA implementation uses the fast iterative shrinkage-thresholding algorithm (FISTA) (Beck and Teboulle 2009). See the bottom plots in Figure 1.

On the one hand, LARS is a homotopy approach that computes all the possible solutions to the optimization problem and their corresponding value of λ , i.e., the regularization path, and the solution according to the Bayesian Information Criterion (BIC) (Schwarz 1978) was recommended as the most appropriate in the case of PFM approaches (Gaudes et al. 2013; Caballero-Gaudes et al. 2019).

Alternatively, the regularization parameter λ can also be updated in every iteration of the FISTA so that the residuals of the data fit converge to a previously estimated noise level of the data $\hat{\sigma}$:

$$\lambda^{n+1} = \frac{N\hat{\sigma}}{\frac{1}{2}\|\mathbf{y} - \mathbf{x}^n\|_F^2} \lambda^n, \quad (9)$$

where x^n is the n^{th} iteration estimate, λ^n and λ^{n+1} are the n^{th} and $n+1^{th}$ iteration values for the regularization parameter λ , and N is the number of points in the time-course. This pre-estimated noise level can be calculated as the median absolute deviation (MAD) of the fine-scale wavelet

130 coefficients (Daubechies, order 3) of the fMRI timecourse. The MAD criterion has been adopted in TA (Karahanoglu et al. 2013). Of note, similar formulations based on the MAD estimate have also been applied in PFM formulations (Gaudes et al. 2012, 2011).

3. Methods

3.1. Simulated data

In order to compare the two methods while controlling for their correct performance, we created a simulation scenario that can be found in the GitHub repository shared in section 6. For the sake of illustration, we describe here the simulations corresponding to a timecourse with a duration of 400 seconds (TR = 2 s) where the activity-inducing signal includes 5 events, which are convolved it with the canonical HRF. Different noise sources (physiological, thermal, and motion-related) were also added and we simulated three different scenarios with varying signal-to-noise ratios (SNR = [20 dB, 10 dB, 3 dB]) that represent low, medium and high contrast-to-noise ratios as shown in Figure 2A. Noise was created following the procedure in (Gaudes et al. 2013) as the sum of uncorrelated Gaussian noise and sinusoidal signals to simulate a realistic noise model with thermal noise, cardiac and respiratory physiological fluctuations, respectively. The physiological signals were generated as

$$\sum_{i=1}^2 \frac{1}{2^{i-1}} (\sin(2\pi f_{r,i}t + \phi_{r,i}) + \sin(2\pi f_{c,i}t + \phi_{c,i})), \quad (10)$$

135 with up to second-order harmonics per cardiac ($f_{c,i}$) and respiratory ($f_{r,i}$) component that were randomly generated following normal distributions with variance 0.04 and mean if_r and if_c , for $i = [1, 2]$. We set the fundamental frequencies to $f_r = 0.3$ Hz for the respiratory component (Birn et al. 2006) and $f_c = 1.1$ Hz for the cardiac component (Shmueli et al. 2007). The phases of each harmonic ϕ were randomly selected from a uniform distribution between 0 and 2π radians. To 140 simulate physiological noise that is proportional to the change in BOLD signal, a variable ratio between the physiological (σ_P) and the thermal (σ_0) noise was modeled as $\sigma_P/\sigma_0 = a(tSNR)^b + c$, where $a = 5.01 \times 10^{-6}$, $b = 2.81$, and $c = 0.397$, following the experimental measures available in Table 3 in (Triantafyllou et al. 2005).

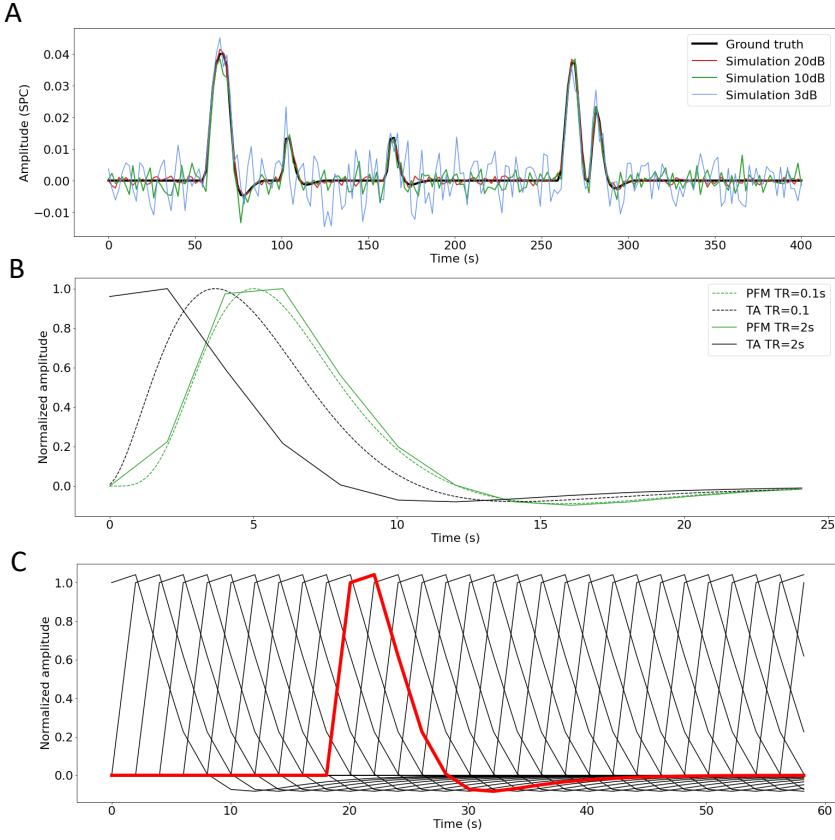


Figure 2: A) Simulated signal with different SNRs (20 dB, 10 dB and 3 dB) and ground truth. B) Canonical HRF models typically used by PFM (green) and TA (black) at TR = 0.1 s (dashed lines) and TR = 2 s (solid lines). Without loss of generality, the waveforms are scaled to unit amplitude for visualization. C) Representation of shifted HRFs at TR = 2 s that build the design matrix for PFM when the HRF model has been matched to that in TA. The red line corresponds to one of the columns of the HRF matrix.

3.2. Experimental data

To compare the performance of the two approaches as well as illustrate their operation, we employ two representative experimental datasets.

Motor task dataset: One healthy subject was scanned in a 3T MR scanner (Siemens) under a Basque Center on Cognition, Brain and Language Review Board-approved protocol. T2*-weighted multi-echo fMRI data was acquired with a simultaneous-multislice multi-echo gradient echo-planar imaging sequence, kindly provided by the Center of Magnetic Resonance Research (University of Minnesota, USA) (Feinberg et al. 2010; Moeller et al. 2010; Setsompop et al. 2011), with the following parameters: 340 scans, 52 slices, Partial-Fourier = 6/8, voxel size = $2.4 \times 2.4 \times 3$ mm³, TR = 1.5 s, TEs = 10.6/28.69/46.78/64.87/82.96 ms, flip angle = 70°, multiband factor = 4, GRAPPA = 2. During the fMRI acquisition, subjects performed a motor task consisting of five different movements (left-hand finger tapping, right-hand finger tapping, moving the left toes, moving the right toes and moving the tongue) that were visually cued through a mirror located on the head coil.

These conditions were randomly intermixed every 16 seconds, and were only repeated once the entire set of stimuli were presented. Data preprocessing in AFNI and TEDANA (Community et al. 2021) consisted of optimally combining the echo time datasets, detrending of up to 5th-order Legendre polynomials, within-brain spatial smoothing (3 mm FWHM) and voxelwise signal normalization to percentage change. The onset and duration of the different conditions can be seen in Figure 5, along with the time-series of representative voxels located in the motor areas corresponding to each of the conditions.

Resting-state datasets: One healthy subject was scanned in a 3T MR scanner (Siemens) under a Basque Center on Cognition, Brain and Language Review Board-approved protocol. Two runs of T2*-weighted fMRI data were acquired during resting-state, each with 10 min duration, with 1) a standard gradient-echo echo-planar imaging sequence (monoband) (TR = 2000 ms, TE = 29 ms, flip-angle = 78°, matrix size = 64 × 64, voxel size = 3 × 3 × 3 mm³, 33 axial slices with interleaved acquisition, slice gap = 0.6 mm) and 2) a simultaneous-multislice gradient-echo echo-planar imaging sequence (multiband factor = 3, TR = 800 ms, TE = 29 ms, flip-angle = 60°, matrix size = 64 × 64, voxel size = 3 × 3 × 3 mm³, 42 axial slices with interleaved acquisition, no slice gap). Single-band reference images were also collected in both resting-state acquisitions for head motion realignment. Field maps were also obtained to correct for field distortions.

During both acquisitions, participants were instructed to keep their eyes open, fixating a white cross that they saw through a mirror located on the head coil, and not think about anything specific. The data was pre-processed using AFNI (Cox 1996). First, volumes corresponding to the initial 10 seconds were removed to allow for a steady-state magnetization. Then, the voxel time-series were despiked to reduce large-amplitude deviations and slice-time corrected. Inhomogeneities caused by magnetic susceptibility were corrected with FUGUE (FSL) using the field map images (Jenkinson et al. 2012). Next, functional images were realigned to a base volume (monoband: volume with the lowest head motion; multiband: single-band reference image). Finally, a simultaneous nuisance regression step was performed comprising up to 6th-order Legendre polynomials, low-pass filtering with a cutoff frequency of 0.25 Hz (only on multiband data to match the frequency content of the monoband), 6 realignment parameters plus temporal derivatives, 5 principal components of white matter (WM), 5 principal components of lateral ventricle voxels (anatomical CompCor) and 5 principal components of the brain's edge voxels. WM, CSF and brain's edge-voxel masks were obtained from Freesurfer tissue and brain segmentations. In addition, scans with potential artifacts were identified and censored when the euclidean norm of the temporal derivative of the realignment parameters (ENORM) was larger than 0.4, and the proportion of voxels adjusted in the despiking step exceeded 10%.

3.3. Selection of the hemodynamic response function

By default, PFM and TA employ different shapes of the discrete-time hemodynamic response functions to estimate neuronal-related signals: the canonical HRF in the case of PFM, and an HRF resulting from the linear differential operator \mathbf{D}_H in the case of TA. Their temporal patterns are shown in Figure 2B. Consequently, to ensure a fair comparison between the two methods, we build the synthesis operator \mathbf{H} with shifted versions of the HRF given by the analysis operator (see Figure 2C) taking advantage of its versatile structure.

3.4. Selection of the regularization parameter

We use the simulated data to compare the performance of the two deconvolution algorithms with both BIC and MAD criteria to choose the regularization parameter λ (see section 2.6). We

check pre-processing: geometric distortions, steady-state magnetization, realignment, elastic

Maybe we need to cite the aCompCor paper and Patriat for the brain's edge voxels. We have already many references though. Opinions?

also evaluate if the algorithms behave differently in terms of the estimation of the activity-inducing signal \hat{s} using the spike model described in Eq. (4) and the block model based on the innovation signal \hat{u} in (8).

For selection based on the BIC, LARS was initially performed with the PFM deconvolution model to obtain the solution for every possible λ in the regularization path. Then, the values of λ corresponding to the BIC solution was adopted to solve the TA deconvolution model by means of FISTA.

For a selection based on the MAD estimate of the noise, we apply the temporal regularization in its original form for TA, whereas for PFM the selected λ corresponds to the solution whose residuals have the closest standard deviation to the estimated noise level of the data $\hat{\sigma}$.

3.5. Analyses in experimental fMRI data

Difference between approaches: To assess the extent of the discrepancies between both approaches when applied on experimental fMRI data, we calculate the sum of squares of the differences (SSD) between the activity-inducing signals estimated with PFM and TA on the three experimental datasets as

$$SSD = \frac{\sum_k (\hat{s}_{\text{PFM}}[k] - \hat{s}_{\text{TA}}[k])^2}{N}, \quad (11)$$

where N is the number of timepoints of the acquisition. The SSD of the innovation signals \hat{u} was computed equally.

Task fMRI data: In the analysis of the motor task data, we evaluate the performance of PFM and TA in comparison with a conventional General Linear Model analysis (*3dDeconvolve* in AFNI) that takes advantage of the information about the duration and onsets of the motor trials. Given the block design of the motor task, we only make this comparison with the block model.

Resting-state fMRI data: We also illustrate the usefulness of deconvolution approaches in the analysis of resting state data where information about the timings of neuronal-related BOLD activity cannot be predicted. Apart from being able to explore individual maps of deconvolved activity (i.e. innovation signals, activity-inducing signal or hemodynamic signals) at the temporal resolution of the acquisition (or deconvolution), here we calculate the co-activation patterns (CAPs) and innovation-driven co-activation patterns (iCAPs) from the obtained activity-inducing and innovation signals. To achieve this, we calculate the average time-series in a seed of 9 voxels located in the precuneus, supramarginal gyrus and occipital gyri independently, and solve the deconvolution problem to find the activity-inducing and innovation signals in the seeds. We then apply a 95th percentile threshold and average the maps of the time-frames that survive the threshold. Finally, we apply the same procedure to the original— i.e., non-deconvolved— signal in the seed and compare the results with the widely-used seed correlation approach.

4. Results

4.1. Performance based on the regularization parameter

Figure 3A shows the regularization paths of PFM and TA side by side obtained for the spike model in Eq. (4) for SNR=3 dB. The solutions for all three SNR conditions are shown in Figure S1 and S2. Starting from the maximum λ corresponding to a null estimate and for decreasing values of λ , LARS computes a new estimate at the value of λ that reduces the sparsity promoted by the l_1 -norm and causes a change in the active set of non-zero coefficients of the estimate (i.e. a

zero coefficient becomes non-zero or viceversa) as shown in the x-axis of the heatmaps. Vertical black lines depict the selection of the regularization parameter based on BIC, and thus, the colored coefficients indicated by the vertical lines depict the estimated activity-inducing signal \hat{s} . Figure 3B illustrates the resulting estimates of the activity-inducing and activity-related hemodynamic signals when basing the selection of λ on BIC for SNR=3 dB. Given that the regularization paths of both approaches are identical, it can be clearly observed that the BIC-based estimates are identical too for the corresponding λ . Thus, Figure 3A and B demonstrate that, regardless of the simulated SNR condition, the spike model of both deconvolution algorithms produce identical regularization paths when the same HRF and regularization parameters are applied, and hence, identical estimates of the activity-inducing signal \hat{s} and neuronal-related hemodynamic signal \hat{x} . Likewise, Figure 3C demonstrates that the regularization paths for the block model defined in Eqs. (7) and (8) also yield virtually identical estimates of the innovation signals for both PFM and TA methods. Again, the BIC-based selection of λ is identical for both PFM and TA. As illustrated in Figure 3D, the estimates of the innovation signal u also show no distinguishable differences between the algorithms. Hence, Figures 3 A-D demonstrate that both PFM and TA yield equivalent regularization paths and estimates of the innovation signal and activity-inducing signal regardless of the simulated SNR condition when applying the same HRF and regularization parameters with the block and spike models.

As for selecting λ with the MAD criterion defined in (9), Figure 3E depicts the estimated activity-inducing, innovation, and activity-related signals for the three simulated SNR settings using the spike model, while Figure 3F shows the estimated signals corresponding to the block model. Both plots in Figure 3E and F depict nearly identical results between PFM and TA with both models. Given that the regularization paths of both techniques are identical, minor differences are owing to the slight dissimilarities in the convergence of the residuals to the estimated noise level of the data.

Last sentence could be skipped and moved to a general conclusion paper in the discussion

4.2. Performance on experimental data

Figure 4 depicts the sum of squares difference (SSD) between PFM and TA estimates of the spike (Figure 4A and C) and block (Figure 4B and D) models for the three experimental fMRI datasets. The SSD values are virtually negligible (i.e. depicted in yellow) in most of the within-brain voxels and clearly lower than the amplitude of the estimates of the activity-inducing and innovation signals. Based on the maximum value of the range shown in each image, we observe that the similarity between both approaches is more evident for the spike model (with both selection criteria) and the block model with the BIC selection. However, a selection of the regularization parameter λ based on the MAD estimate of the noise using the block model produces higher SSD values, with the largest differences occur in regions with high vasculature likely owing to the high levels of noise in these voxels. These areas also correspond to the highest values of λ (see Supplementary Figure S3) and the highest MAD estimates of the noise (see Supplementary Figure S4).

Do we need to expand more on the interpretation of this Figure?

Figure 5 depicts the results of the analysis of the Motor dataset with the PFM and TA algorithms using the BIC selection of λ (see Figure S5 for results with MAD selection), as well as a conventional GLM approach. The Activation Time Series (top left), calculated as the sum of squares of all voxel amplitudes (positive vs. negative) for a given moment in time, obtained with PFM and TA show nearly identical patterns. These ATS help to summarize the four dimensional information available in the results across the spatial domain and identify instances of significant BOLD activity. The differences observed with the block model and a selection of λ based on the MAD estimate shown

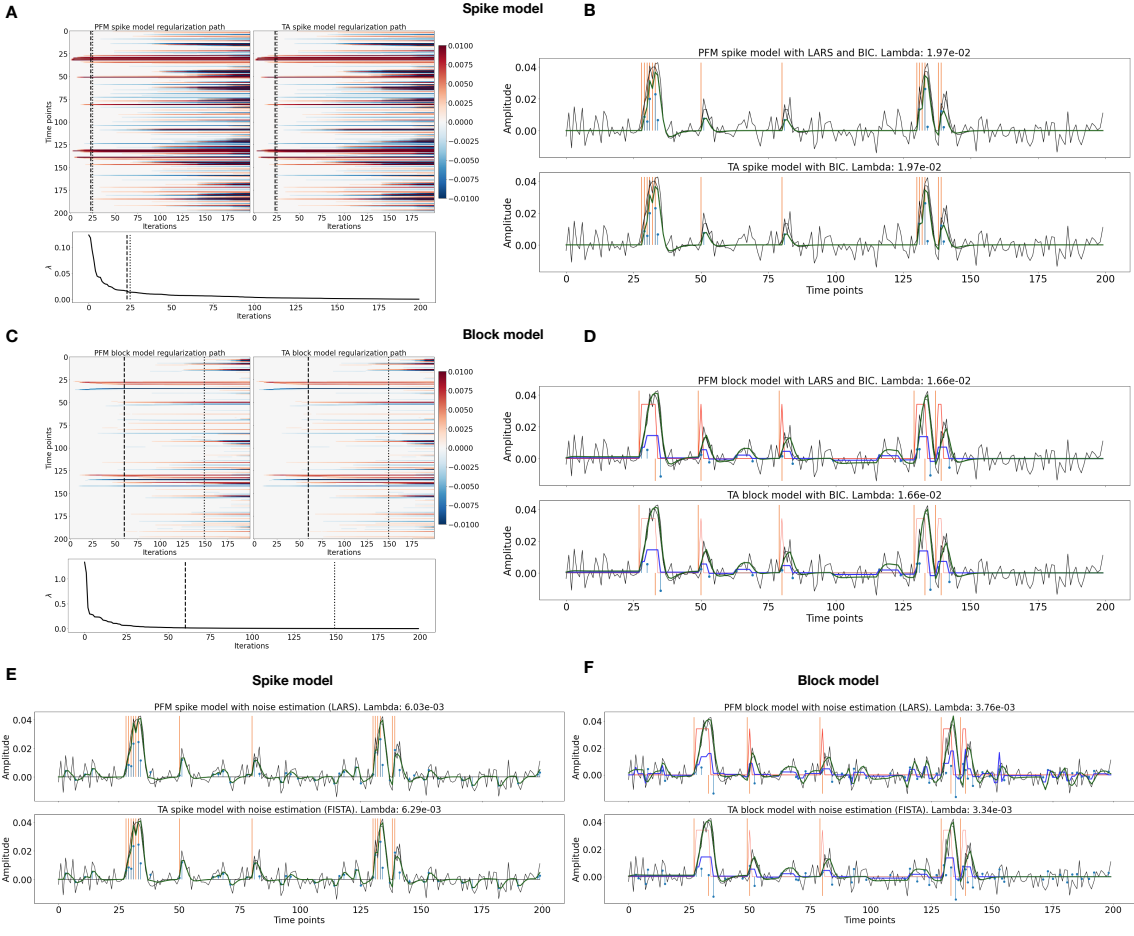


Figure 3: (A) Heatmap of the regularization paths of the activity-inducing signals (spike model) estimated with PFM and TA as a function of λ for the simulated data with SNR = 3 dB (x-axis: increasing number of iterations or λ as given by LARS; y-axis: time; color: amplitude). Vertical lines denote iterations corresponding to the BIC (dashed line) and MAD (dotted line) selection of λ . (B) Estimated activity-inducing (blue) and activity-related (green) signals with a selection of λ based on BIC. (C) Heatmap of the regularization paths of the innovation signals (block model) estimated with PFM and TA as a function of λ for the simulated data with SNR = 3 dB. (D) Estimated innovation (blue), activity-inducing (darker blue), and activity-related (green) signals with a selection of λ based on BIC. (E) Estimated activity-inducing, innovation and activity-related (fit, \times) signals estimated with PFM (top) and TA (bottom) when λ is selected based on the MAD method with the spike model, and (F) with the block model for the simulated data with SNR = 3 dB.

in Figure 4 are reflected on the ATS shown in Figure S5. The rows below show the voxel timeseries and the corresponding activity-related, activity-inducing and innovation signals obtained with PFM using the BIC criterion of representative voxels in the regions activated in each of the motor tasks. The TA-estimated time-series are not shown because they were equivalent. The maps shown on the right correspond to statistical parametric map obtained with the GLM for each motor condition ($p < 0.001$) as well as the maps of the PFM and TA estimates at the onsets of individual motor

285

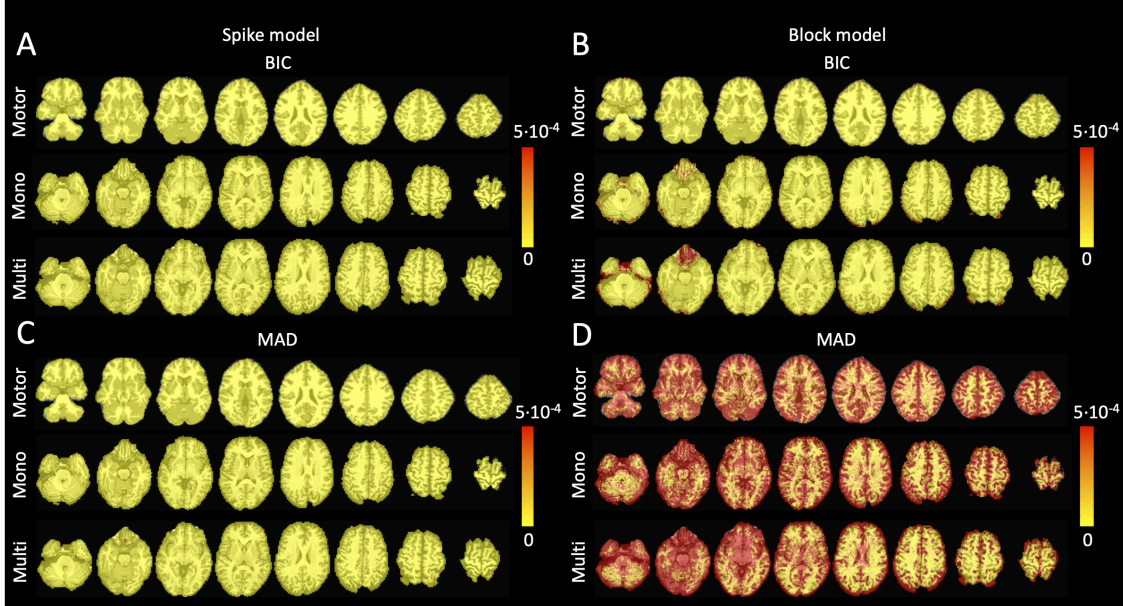


Figure 4: Sum of squares of the differences (SSD) between the estimates obtained with PFM and TA for (A) spike model (activity-inducing signal) and BIC selection of λ , (B) block model (innovation signal) and BIC, (C) spike model (activity-inducing signal) and MAD, (D) block model (innovation signal) and MAD. SSD maps are shown for the three experimental fMRI datasets: the motor task (Motor), the monoband resting-state (Mono), and the multiband resting-state (Multi) datasets.

events (indicated with arrows in the timecourse). The estimated activity-related, activity-inducing and innovation signals clearly reveal the activity patterns of each condition in the task, as they exhibit a BOLD response locked to the onset and duration of the conditions. Overall, activity maps of the innovation signal obtained with PFM and TA highly resemble those obtained with a GLM for individual events.

As an illustration of the insights that deconvolution methods can provide in the analysis of resting-state data, Figure 6 depicts the CAPs and iCAPs obtained from thresholding and averaging the activity-inducing and innovation signals, respectively, estimated from the resting-state multi-band data using PFM with a selection of λ based on the BIC. The activity-inducing CAPs obtained via deconvolution show spatial patterns of the default mode network (DMN), dorsal attention network (DAN) and visual network (VIS) that highly resemble the maps obtained with conventional seed correlation analysis using Pearson correlation, and the CAPs based on the amplitude of the signal (i.e. with no deconvolution). With deconvolution, the CAPs seem to depict less spurious voxels (mainly negative) and more accurate spatial delineation (i.e. less smoothness) than those obtained from the original data, while maintaining the structure of the networks. The BIC-informed selection of λ yields spatial patterns of CAPs and iCAPs that are more sparse than those obtained with a selection of λ based on the MAD estimate (see Supplementary Figure S6). On the other hand, the spatial patterns of the iCAPs based on the innovation signals using the block model yield complementary information to that obtained with the activity-inducing signal since iCAPs allows to reveal regions with synchronous innovations, i.e. with the same upregulating and downregulating

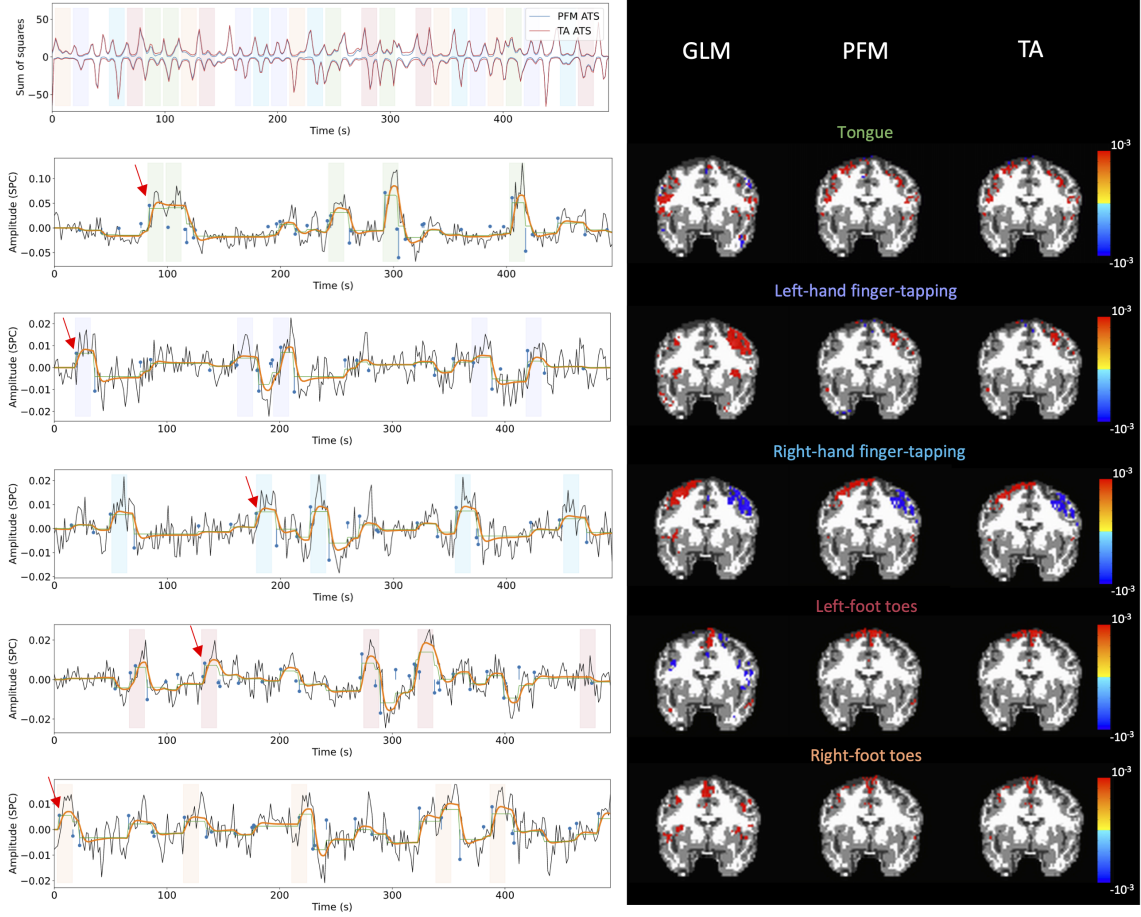


Figure 5: Activity maps of the motor task using a selection of λ based on the BIC estimate. Row 1: Activation time-series of the innovation signals estimated by PFM (in blue) or TA (in red) calculated as the sum of squares of all voxels at every timepoint. Positive-valued and negative-valued contributions were separated into two distinct time-courses. Color-bands indicate the onset and duration of each condition in the task (green: tongue, purple: left-hand finger-tapping, blue: right-hand finger-tapping, red: left-foot toes, orange: right-foot toes). Rows 2-6: time-series of a representative voxel for each task with the PFM-estimated innovation (blue), PFM-estimated activity-inducing (green), and activity-related (i.e., fitted, orange) signals, with their corresponding GLM, PFM, and TA maps on the right. The maps shown on the right are sampled at the time-point labeled with the red arrows and display the innovation signals at that moment across the whole brain.

events. For instance, it is interesting to observe that the structure of the visual network nearly disappears in its corresponding iCAPs, suggesting the existence of different temporal neuronal patterns across voxels in the primary and secondary visual cortices.

Should we discuss something about computational time?

310

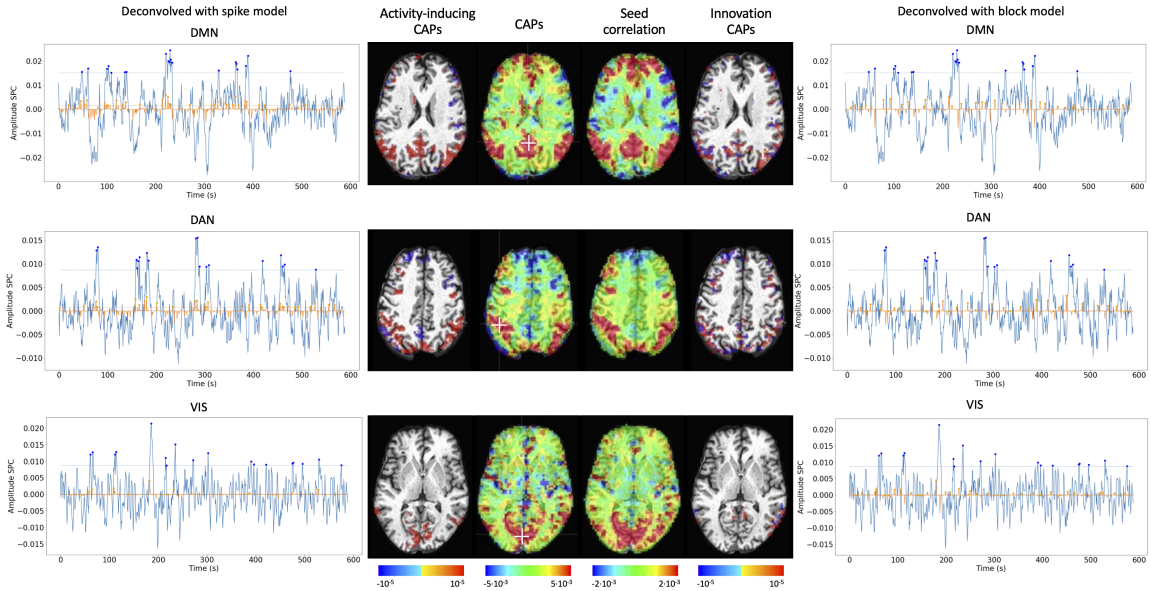


Figure 6: Activity-inducing CAPs (left) and innovation CAPs (right) obtained with the PFM-estimated activity-inducing and innovation signals respectively, using a BIC-based selection of λ . Time-points selected with a 95th percentile threshold are shown over the average time-series (blue) in the seed region (white-cross) and the deconvolved signal (orange). CAPs and seed correlation maps are illustrated in the center.

5. Discussion

This work demonstrates that PFM and TA algorithms yield practically identical results when the same HRF model and equivalent regularization parameters are employed, showing that synthesis and analysis-based formulations are comparable for temporal hemodynamic deconvolution of fMRI data under a linear-time invariant model of the neurovascular coupling. Hence, we argue that previously observed differences in performance can be explained in terms of differences in usage options, such as the specific HRF model and selection of the regularization parameter, convergence thresholds, as well as the addition of a spatial regularization term in the TA formulation described in Karahanoglu et al. 2013. With the equivalence in the temporal deconvolution demonstrated, incorporating extra spatial or temporal regularization terms in the optimization problem would not modify this equivalence providing convex operators are employed. In terms of convergence, this equivalence is particularly relevant when the optimization problem is convex (i.e. with a unique global solution) and is solved by means of iterative shrinkage thresholding procedures that alternate between the different regularization terms of the functional, such as the Generalized Forward-Backward Splitting (Raguet et al. 2013) algorithm originally employed for TA. Our findings are in line with the equivalence of analysis and synthesis methods in under-determined cases ($N \leq V$) demonstrated in (Elad et al. 2007) and (Ortelli and van de Geer 2019).

Nevertheless, the differences between analysis and synthesis deconvolution models must be considered to achieve optimal performance with any research question in hand. For instance, while TA uses the same HRF to solve both the spike and block models using the Generalized Total Variation

Do you think we need to discuss the small differences observed with the block model for the MAD criterion?

formulation (Karahanoglu et al. 2011), PFM incorporates the discrete differentiator operator into forward model along with the HRF to estimate innovation signals. The more flexible approach adopted by PFM offers the advantage that the synthesis operator allows for any HRF shape (Elad et al. 2007), only requiring that the coefficients are given at the desired temporal resolution of the deconvolved estimates, which is typically equal to the TR of the acquisition. Given its more intuitive and versatile structure, the synthesis formulation proposed by PFM can easily be extended for deconvolution of multiple fMRI inputs with a common neuronal-related signal, for example for the estimation of neuronal-related events on multi-echo data (Caballero-Gaudes et al. 2019).

Dimitri: Do you agree that a multivariate deconvolution as in multi-echo would be more difficult to formulate with the total variation formulation?

At the same time, deconvolution techniques can be used prior to the analysis of functional networks as they estimate interactions between brain regions that occur at the neuronal level, which are significantly less affected the sluggishness of the hemodynamic response and confounding effects than directly analyzing hemodynamic interactions. (Gitelman et al. 2003)

Should we delete this sentence?

In addition, deconvolution approaches have a close parallelism to recent methodologies aiming to understand the dynamics of neuronal activations and interactions at short temporal resolution and that focus on extreme events in the fMRI signal. As an illustration, Figure 6 shows that the innovation- or activity-inducing CAPs computed from deconvolved events in a single resting-state fMRI dataset closely resemble the conventional CAPs computed directly from extreme events of the fMRI signal (Liu and Duyn 2013; Liu et al. 2013, 2018; Cifre et al. 2020a,b; Zhang et al. 2020; Tagliazucchi et al. 2011, 2012, 2016; Rolls et al. 2021). Similarly, we hypothesize that these extreme events will also show a close resemblance to intrinsic ignition events (Deco and Kringelbach 2017; Deco et al. 2017). As shown in the maps, deconvolution approaches can offer a more straightforward interpretability of the activation events and resulting functional connectivity patterns. For the sake of illustration, CAPs were computed here as the average of spatial maps corresponding to the events of a single dataset. Beyond simple averaging, other clustering algorithms (e.g. K-means, consensus clustering) can be employed to discern multiple CAPs at the whole-brain level when a larger number of subjects or datasets is available (Karahanoglu and Ville 2015). Likewise, the dynamics of functional connectivity have recently been investigated with the use of co-fluctuations and edge-centric techniques (Faskowitz et al. 2020; Esfahlani et al. 2020; Jo et al. 2021; Sporns et al. 2021; van Oort et al. 2018). The Activation Time Series shown in Figure 5 aim to offer equivalent information to the root of sum of squares timecourses used in edge-centric approaches as timecourses with peaks that delineate instances of significant brain activity. Future work could address which type of information is redundant or distinct across these frameworks. In summary, these examples illustrate that deconvolution techniques can be employed prior to other computational approaches and could serve as an effective way of denoising the fMRI data. We foresee an increase in the number of studies that take advantage of the potential benefits of using deconvolution methods prior to functional connectivity analyses.

Finally, taking into account the equivalent performance of analysis and synthesis deconvolution approaches, it is clear that fMRI deconvolution methods still have room for improvement and their capabilities can be extended to reach a wider community of researchers. Of particular relevance are deconvolution formulations aiming to account for HRF variability, for example using structured regularization terms along with multiple basis functions (Gaudes et al. 2012) or iterative procedures that estimate the HRF shape in an iterative fashion (Farouj et al. 2019; Cherkaoui et al. 2020).

Dimitri,
could you
write a sentence about
the requirements for
the HRF
filter, for instance that
the hemodynamic operator
must be defined
in terms of
zeros and
poles

³⁷⁵ Another venue of research are multivariate deconvolution approaches that operate at the whole-brain level, instead of voxelwise, for instance using low rank decompositions (Cherkaoui et al. 2020) or group (a.k.a. mixed norm) regularization terms (Uruñuela-Tremiño et al. 2019). Methods for a more robust selection of the regularization parameter could also be explored, for instance based on stability selection (Meinshausen and Bühlmann 2010; Uruñuela et al. 2020). Furthermore, the use
³⁸⁰ of non-convex $\ell_{p,q}$ -norm regularization terms (e.g., $p < 1$) could avoid the extra debiasing step that is necessary to overcome the shrinkage towards zero of the estimates and obtain a more accurate and less biased fit of the fMRI signal (Gaudes et al. 2013; Caballero-Gaudes et al. 2019). Alternatively, recent developments on physics-informed deep learning for inverse problems (Akçakaya et al. 2021; Monga et al. 2021; Ongie et al. 2020) could become an interesting venue of research to reduce the
³⁸⁵ computational time and gain flexibility.

6. Code and data availability

The code and materials used in this work can be found in the following GitHub repository: https://github.com/eurunuela/pfm_vs_ta. We encourage the reader to explore the parameters (e.g. SNR, varying HRF options and mismatch between algorithms, TR, number of events, onsets, and durations) in the provided Jupyter notebooks. Likewise, the data used to produce the figures can be found in <https://osf.io/f3ryg/>.

7. Acknowledgements

This research was funded by the European Union's Horizon 2020 research and innovation program (agreement No. 713673 of the Marie Skłodowska-Curie grant), La Caixa Foundation (ID 100010434, fellowship code LCF/BQ/IN17/11620063), the Spanish Ministry of Economy and Competitiveness (RYC-2017-21845), the Basque Government (BERC 2018-2021, PIBA_2019_104, PRE_2019_1_005 4), and the Spanish Ministry of Science, Innovation and Universities (PID2019-105520GB-100).

References

- ⁴⁰⁰ Akçakaya, M., Yaman, B., Chung, H., Ye, J.C., 2021. Unsupervised deep learning methods for biological image reconstruction [arXiv:2105.08040](https://arxiv.org/abs/2105.08040).
- Allan, T.W., Francis, S.T., Caballero-Gaudes, C., Morris, P.G., Liddle, E.B., Liddle, P.F., Brookes, M.J., Gowland, P.A., 2015. Functional connectivity in MRI is driven by spontaneous BOLD events. PLOS ONE 10, e0124577. doi:10.1371/journal.pone.0124577.
- ⁴⁰⁵ Aslan, S., Cemgil, A.T., Akin, A., 2016. Joint state and parameter estimation of the hemodynamic model by particle smoother expectation maximization method. Journal of Neural Engineering 13, 046010. doi:10.1088/1741-2560/13/4/046010.
- Beck, A., Teboulle, M., 2009. A fast iterative shrinkage-thresholding algorithm for linear inverse problems. SIAM Journal on Imaging Sciences 2, 183–202. doi:10.1137/080716542.
- ⁴¹⁰ Birn, R.M., Diamond, J.B., Smith, M.A., Bandettini, P.A., 2006. Separating respiratory-variation-related fluctuations from neuronal-activity-related fluctuations in fMRI. NeuroImage 31, 1536–1548. doi:10.1016/j.neuroimage.2006.02.048.

- Bolton, T.A., Morgenroth, E., Preti, M.G., Ville, D.V.D., 2020. Tapping into multi-faceted human behavior and psychopathology using fMRI brain dynamics. *Trends in Neurosciences* 43, 667–680. doi:10.1016/j.tins.2020.06.005.
- 415 Bommarito, G., Tarun, A., Farouj, Y., Preti, M.G., Petracca, M., Droby, A., Mendili, M.M.E., Inglese, M., Ville, D.V.D., 2020. Altered anterior default mode network dynamics in progressive multiple sclerosis. medRxiv doi:10.1101/2020.11.26.20238923.
- 420 Boynton, G.M., Engel, S.A., Glover, G.H., Heeger, D.J., 1996. Linear systems analysis of functional magnetic resonance imaging in human v1. *The Journal of Neuroscience* 16, 4207–4221. doi:10.1523/jneurosci.16-13-04207.1996.
- Bruckstein, A.M., Donoho, D.L., Elad, M., 2009. From sparse solutions of systems of equations to sparse modeling of signals and images. *SIAM Review* 51, 34–81. doi:10.1137/060657704.
- 425 Bush, K., Cisler, J., 2013. Decoding neural events from fMRI BOLD signal: A comparison of existing approaches and development of a new algorithm. *Magnetic Resonance Imaging* 31, 976–989. doi:10.1016/j.mri.2013.03.015.
- Bush, K., Zhou, S., Cisler, J., Bian, J., Hazaroglu, O., Gillispie, K., Yoshigoe, K., Kilts, C., 2015. A deconvolution-based approach to identifying large-scale effective connectivity. *Magnetic Resonance Imaging* 33, 1290–1298. doi:10.1016/j.mri.2015.07.015.
- 430 Buxton, R.B., Wong, E.C., Frank, L.R., 1998. Dynamics of blood flow and oxygenation changes during brain activation: the balloon model. *Magnetic resonance in medicine* 39, 855–864.
- Caballero-Gaudes, C., Moia, S., Panwar, P., Bandettini, P.A., Gonzalez-Castillo, J., 2019. A deconvolution algorithm for multi-echo functional MRI: Multi-echo sparse paradigm free mapping. *NeuroImage* 202, 116081. doi:10.1016/j.neuroimage.2019.116081.
- 435 Chambolle, A., 2004. An algorithm for total variation minimization and applications. *Journal of Mathematical imaging and vision* 20, 89–97.
- Chen, S.S., Donoho, D.L., Saunders, M.A., 2001. Atomic decomposition by basis pursuit. *SIAM review* 43, 129–159.
- 440 Cherkaoui, H., Moreau, T., Halimi, A., Ciuciu, P., 2019. Sparsity-based blind deconvolution of neural activation signal in fMRI, in: ICASSP 2019 - 2019 IEEE International Conference on Acoustics, Speech and Signal Processing (ICASSP), IEEE. pp. 1323–1327. doi:10.1109/icassp.2019.8683358.
- Cherkaoui, H., Moreau, T., Halimi, A., Leroy, C., Ciuciu, P., 2020. Multivariate semi-blind deconvolution of fMRI time series. URL: <https://hal.archives-ouvertes.fr/hal-03005584>. working paper or preprint.
- 445 Cifre, I., Flores, M.T.M., Ochab, J.K., Chialvo, D.R., 2020a. Revisiting non-linear functional brain co-activations: directed, dynamic and delayed. arXiv:2007.15728.
- Cifre, I., Zarepour, M., Horovitz, S.G., Cannas, S.A., Chialvo, D.R., 2020b. Further results on why a point process is effective for estimating correlation between brain regions. *Papers in Physics* 12, 120003. doi:10.4279/pip.120003.

- Cohen, M.S., 1997. Parametric analysis of fMRI data using linear systems methods. *NeuroImage* 6, 93–103. doi:10.1006/nimg.1997.0278.
- Community, T.T., Ahmed, Z., Bandettini, P.A., Bottenhorn, K.L., Caballero-Gaudes, C., Dowdle, L.T., DuPre, E., Gonzalez-Castillo, J., Handwerker, D., Heunis, S., Kundu, P., Laird, A.R., 455 Markello, R., Markiewicz, C.J., Maullin-Sapey, T., Moia, S., Salo, T., Staden, I., Teves, J., Uruñuela, E., Vaziri-Pashkam, M., Whitaker, K., 2021. Me-ica/tedana: 0.0.10. doi:10.5281/ZENODO.4725985.
- Costantini, I., Deriche, R., Deslauriers-Gauthier, S., 2021. A paradigm free regularization approach to recover brain activation from functional MRI data. *bioRxiv* doi:10.1101/2021.04.14.438942.
- 460 Cox, R.W., 1996. AFNI: Software for analysis and visualization of functional magnetic resonance neuroimages. *Computers and Biomedical Research* 29, 162–173. doi:10.1006/cbmr.1996.0014.
- Deco, G., Kringelbach, M.L., 2017. Hierarchy of information processing in the brain: A novel 'intrinsic ignition' framework. *Neuron* 94, 961–968. doi:10.1016/j.neuron.2017.03.028.
- 465 Deco, G., Tagliazucchi, E., Laufs, H., Sanjuán, A., Kringelbach, M.L., 2017. Novel intrinsic ignition method measuring local-global integration characterizes wakefulness and deep sleep. *eNeuro* 4. doi:10.1523/ENEURO.0106-17.2017.
- Di, X., Biswal, B.B., 2013. Modulatory interactions of resting-state brain functional connectivity. *PLoS ONE* 8, e71163. doi:10.1371/journal.pone.0071163.
- 470 Di, X., Biswal, B.B., 2015. Characterizations of resting-state modulatory interactions in the human brain. *Journal of Neurophysiology* 114, 2785–2796. doi:10.1152/jn.00893.2014.
- Di, X., Biswal, B.B., 2018. Toward task connectomics: Examining whole-brain task modulated connectivity in different task domains. *Cerebral Cortex* 29, 1572–1583. doi:10.1093/cercor/bhy055.
- Efron, B., Hastie, T., Johnstone, I., Tibshirani, R., 2004. Least angle regression. *The Annals of Statistics* 32, 407–499. doi:10.1214/009053604000000067.
- 475 Elad, M., Milanfar, P., Rubinstein, R., 2007. Analysis versus synthesis in signal priors. *Inverse Problems* 23, 947–968. doi:10.1088/0266-5611/23/3/007.
- Esfahlani, F.Z., Jo, Y., Faskowitz, J., Byrge, L., Kennedy, D.P., Sporns, O., Betzel, R.F., 2020. High-amplitude cofluctuations in cortical activity drive functional connectivity. *Proceedings of the National Academy of Sciences* 117, 28393–28401. doi:10.1073/pnas.2005531117.
- 480 Farouj, Y., Karahanoglu, F.I., Ville, D.V.D., 2019. Bold signal deconvolution under uncertain hEModynamics: A semi-blind approach, in: 2019 IEEE 16th International Symposium on Biomedical Imaging (ISBI 2019), IEEE. IEEE. pp. 1792–1796. doi:10.1109/isbi.2019.8759248.
- Faskowitz, J., Esfahlani, F.Z., Jo, Y., Sporns, O., Betzel, R.F., 2020. Edge-centric functional network representations of human cerebral cortex reveal overlapping system-level architecture. *Nature neuroscience* 23, 1644–1654. doi:10.1038/s41593-020-00719-y.

- Feinberg, D.A., Moeller, S., Smith, S.M., Auerbach, E., Ramanna, S., Glasser, M.F., Miller, K.L., Ugurbil, K., Yacoub, E., 2010. Multiplexed echo planar imaging for sub-second whole brain fMRI and fast diffusion imaging. *PLoS ONE* 5, e15710. doi:10.1371/journal.pone.0015710.
- 490 Freitas, L.G., Bolton, T.A., Krikler, B.E., Jochaut, D., Giraud, A.L., Hüppi, P.S., Ville, D.V.D., 2020. Time-resolved effective connectivity in task fMRI: Psychophysiological interactions of co-activation patterns. *NeuroImage* 212, 116635. doi:10.1016/j.neuroimage.2020.116635.
- Friston, K., Fletcher, P., Josephs, O., Holmes, A., Rugg, M., Turner, R., 1998. Event-related fMRI: Characterizing differential responses. *NeuroImage* 7, 30–40. doi:10.1006/nimg.1997.0306.
- 495 Friston, K., Trujillo-Barreto, N., Daunizeau, J., 2008. DEM: A variational treatment of dynamic systems. *NeuroImage* 41, 849–885. doi:10.1016/j.neuroimage.2008.02.054.
- Friston, K.J., Jezzard, P., Turner, R., 1994. Analysis of functional MRI time-series. *Human Brain Mapping* 1, 153–171. doi:10.1002/hbm.460010207.
- 500 Friston, K.J., Mechelli, A., Turner, R., Price, C.J., 2000. Nonlinear responses in fmri: the balloon model, volterra kernels, and other hemodynamics. *NeuroImage* 12, 466–477.
- Gaudes, C.C., Karahanoglu, F.I., Lazeyras, F., Ville, D.V.D., 2012. Structured sparse deconvolution for paradigm free mapping of functional MRI data, in: 2012 9th IEEE International Symposium on Biomedical Imaging (ISBI), IEEE. IEEE. pp. 322–325. doi:10.1109/isbi.2012.6235549.
- 505 Gaudes, C.C., Petridou, N., Dryden, I.L., Bai, L., Francis, S.T., Gowland, P.A., 2010. Detection and characterization of single-trial fMRI bold responses: Paradigm free mapping. *Human Brain Mapping* 32, 1400–1418. doi:10.1002/hbm.21116.
- Gaudes, C.C., Petridou, N., Francis, S.T., Dryden, I.L., Gowland, P.A., 2013. Paradigm free mapping with sparse regression automatically detects single-trial functional magnetic resonance imaging blood oxygenation level dependent responses. *Human Brain Mapping*, n/a–n/adoi:10.1002/hbm.21452.
- 510 Gaudes, C.C., Van De Ville, D., Petridou, N., Lazeyras, F., Gowland, P., 2011. Paradigm-free mapping with morphological component analysis: Getting most out of fmri data, in: Wavelets and Sparsity XIV, International Society for Optics and Photonics. p. 81381K.
- Gerchen, M.F., Bernal-Casas, D., Kirsch, P., 2014. Analyzing task-dependent brain network changes by whole-brain psychophysiological interactions: A comparison to conventional analysis. *Human Brain Mapping* 35, 5071–5082. doi:10.1002/hbm.22532.
- Gitelman, D.R., Penny, W.D., Ashburner, J., Friston, K.J., 2003. Modeling regional and psychophysiological interactions in fMRI: the importance of hemodynamic deconvolution. *NeuroImage* 19, 200–207. doi:10.1016/s1053-8119(03)00058-2.
- 520 Glover, G.H., 1999. Deconvolution of impulse response in event-related BOLD fMRI1. *NeuroImage* 9, 416–429. doi:10.1006/nimg.1998.0419.
- Gonzalez-Castillo, J., Caballero-Gaudes, C., Topolski, N., Handwerker, D.A., Pereira, F., Bandettini, P.A., 2019. Imaging the spontaneous flow of thought: Distinct periods of cognition contribute to dynamic functional connectivity during rest. *NeuroImage* 202, 116129. doi:10.1016/j.neuroimage.2019.116129.

- Havlicek, M., Friston, K.J., Jan, J., Brazdil, M., Calhoun, V.D., 2011. Dynamic modeling of neuronal responses in fMRI using cubature kalman filtering. *NeuroImage* 56, 2109–2128. doi:10.1016/j.neuroimage.2011.03.005.
- Hernandez-Garcia, L., Ulfarsson, M.O., 2011. Neuronal event detection in fMRI time series using iterative deconvolution techniques. *Magnetic Resonance Imaging* 29, 353–364. doi:10.1016/j.mri.2010.10.012.
- Hütel, M., Antonelli, M., Melbourne, A., Ourselin, S., 2021. Hemodynamic matrix factorization for functional magnetic resonance imaging. *NeuroImage* 231, 117814. doi:10.1016/j.neuroimage.2021.117814.
- Hütel, M., Melbourne, A., Ourselin, S., 2018. Neural activation estimation in brain networks during task and rest using BOLD-fMRI, in: Medical Image Computing and Computer Assisted Intervention – MICCAI 2018, Springer. Springer International Publishing. pp. 215–222. doi:10.1007/978-3-030-00931-1_25.
- Jenkinson, M., Beckmann, C.F., Behrens, T.E., Woolrich, M.W., Smith, S.M., 2012. FSL. *NeuroImage* 62, 782–790. doi:10.1016/j.neuroimage.2011.09.015.
- Jo, Y., Faskowitz, J., Esfahlani, F.Z., Sporns, O., Betzel, R.F., 2021. Subject identification using edge-centric functional connectivity. *NeuroImage* 238, 118204. doi:10.1016/j.neuroimage.2021.118204.
- Karahanoğlu, F.I., Bayram, İ., Ville, D.V.D., 2011. A signal processing approach to generalized 1-d total variation. *IEEE Transactions on Signal Processing* 59, 5265–5274. doi:10.1109/tsp.2011.2164399.
- Karahanoğlu, F.I., Caballero-Gaudes, C., Lazeyras, F., Ville, D.V.D., 2013. Total activation: fMRI deconvolution through spatio-temporal regularization. *NeuroImage* 73, 121–134. doi:10.1016/j.neuroimage.2013.01.067.
- Karahanoğlu, F.I., Grouiller, F., Gaudes, C.C., Seeck, M., Vulliemoz, S., Ville, D.V.D., 2013. Spatial mapping of interictal epileptic discharges in fMRI with total activation, in: 2013 IEEE 10th International Symposium on Biomedical Imaging, Ieee. IEEE. pp. 1500–1503. doi:10.1109/isbi.2013.6556819.
- Karahanoğlu, F.I., Ville, D.V.D., 2015. Transient brain activity disentangles fMRI resting-state dynamics in terms of spatially and temporally overlapping networks. *Nature Communications* 6, 7751. doi:10.1038/ncomms8751.
- Karahanoğlu, F.I., Ville, D.V.D., 2017. Dynamics of large-scale fMRI networks: Deconstruct brain activity to build better models of brain function. *Current Opinion in Biomedical Engineering* 3, 28–36. doi:10.1016/j.cobme.2017.09.008.
- Keilholz, S., Caballero-Gaudes, C., Bandettini, P., Deco, G., Calhoun, V., 2017. Time-resolved resting-state functional magnetic resonance imaging analysis: Current status, challenges, and new directions. *Brain Connectivity* 7, 465–481. doi:10.1089/brain.2017.0543.

- Khalidov, I., Fadili, J., Lazeyras, F., Ville, D.V.D., Unser, M., 2011. Activelets: Wavelets for sparse representation of hemodynamic responses. *Signal Processing* 91, 2810–2821. doi:10.1016/j.sigpro.2011.03.008.
- ⁵⁶⁵ Kinany, N., Pirondini, E., Micera, S., Ville, D.V.D., 2020. Dynamic functional connectivity of resting-state spinal cord fMRI reveals fine-grained intrinsic architecture. *Neuron* 108, 424–435.e4. doi:10.1016/j.neuron.2020.07.024.
- Liu, X., Chang, C., Duyn, J.H., 2013. Decomposition of spontaneous brain activity into distinct fMRI co-activation patterns. *Frontiers in Systems Neuroscience* 7, 101. doi:10.3389/fnsys.2013.00101.
- ⁵⁷⁰ Liu, X., Duyn, J.H., 2013. Time-varying functional network information extracted from brief instances of spontaneous brain activity. *Proceedings of the National Academy of Sciences* 110, 4392–4397. doi:10.1073/pnas.1216856110.
- ⁵⁷⁵ Liu, X., Zhang, N., Chang, C., Duyn, J.H., 2018. Co-activation patterns in resting-state fMRI signals. *NeuroImage* 180, 485–494. doi:10.1016/j.neuroimage.2018.01.041.
- Lopes, R., Lina, J., Fahoum, F., Gotman, J., 2012. Detection of epileptic activity in fMRI without recording the EEG. *NeuroImage* 60, 1867–1879. doi:10.1016/j.neuroimage.2011.12.083.
- ⁵⁸⁰ Loula, J., Varoquaux, G., Thirion, B., 2018. Decoding fMRI activity in the time domain improves classification performance. *NeuroImage* 180, 203–210. doi:10.1016/j.neuroimage.2017.08.018.
- Lurie, D.J., Kessler, D., Bassett, D.S., Betzel, R.F., Breakspear, M., Kheilholz, S., Kucyi, A., Liégeois, R., Lindquist, M.A., McIntosh, A.R., Poldrack, R.A., Shine, J.M., Thompson, W.H., Bielczyk, N.Z., Douw, L., Kraft, D., Miller, R.L., Muthuraman, M., Pasquini, L., Razi, A., Vidaurre, D., Xie, H., Calhoun, V.D., 2020. Questions and controversies in the study of time-varying functional connectivity in resting fMRI. *Network Neuroscience* 4, 30–69. doi:10.1162/netn_a_00116.
- ⁵⁸⁵ Madi, M.K., Karameh, F.N., 2017. Hybrid cubature kalman filtering for identifying nonlinear models from sampled recording: Estimation of neuronal dynamics. *PLOS ONE* 12, e0181513. doi:10.1371/journal.pone.0181513.
- ⁵⁹⁰ Meinshausen, N., Bühlmann, P., 2010. Stability selection. *Journal of the Royal Statistical Society: Series B (Statistical Methodology)* 72, 417–473. doi:10.1111/j.1467-9868.2010.00740.x.
- Moeller, S., Yacoub, E., Olman, C.A., Auerbach, E., Strupp, J., Harel, N., Uğurbil, K., 2010. Multiband multislice GE-EPI at 7 tesla, with 16-fold acceleration using partial parallel imaging with application to high spatial and temporal whole-brain fMRI. *Magnetic Resonance in Medicine* 63, 1144–1153. doi:10.1002/mrm.22361.
- ⁵⁹⁵ Monga, V., Li, Y., Eldar, Y.C., 2021. Algorithm unrolling: Interpretable, efficient deep learning for signal and image processing. *IEEE Signal Processing Magazine* 38, 18–44. doi:10.1109/MSP.2020.3016905.
- Ongie, G., Jalal, A., Metzler, C.A., Baraniuk, R.G., Dimakis, A.G., Willett, R., 2020. Deep learning techniques for inverse problems in imaging. *IEEE Journal on Selected Areas in Information Theory* 1, 39–56. doi:10.1109/JSAIT.2020.2991563.

- van Oort, E.S.B., Mennes, M., Navarro Schröder, T., Kumar, V.J., Zaragoza Jimenez, N.I., Grodd, W., Doeller, C.F., Beckmann, C.F., 2018. Functional parcellation using time courses of instantaneous connectivity. *NeuroImage* 170, 31–40. doi:10.1016/j.neuroimage.2017.07.027.
- 605 Ortelli, F., van de Geer, S., 2019. Synthesis and analysis in total variation regularization. [arXiv:1901.06418](https://arxiv.org/abs/1901.06418).
- Petridou, N., Gaudes, C.C., Dryden, I.L., Francis, S.T., Gowland, P.A., 2012. Periods of rest in fMRI contain individual spontaneous events which are related to slowly fluctuating spontaneous activity. *Human Brain Mapping* 34, 1319–1329. doi:10.1002/hbm.21513.
- 610 Pidnebesna, A., Fajnerová, I., Horáček, J., Hlinka, J., 2019. Estimating sparse neuronal signal from hemodynamic response: the mixture components inference approach. *bioRxiv* doi:10.1101/2019.12.19.876508.
- Prete, M.G., Bolton, T.A., Ville, D.V.D., 2017. The dynamic functional connectome: State-of-the-art and perspectives. *NeuroImage* 160, 41–54. doi:10.1016/j.neuroimage.2016.12.061.
- 615 Raguet, H., Fadili, J., Peyré, G., 2013. A generalized forward-backward splitting. *SIAM Journal on Imaging Sciences* 6, 1199–1226. doi:10.1137/120872802.
- Riera, J.J., Watanabe, J., Kazuki, I., Naoki, M., Aubert, E., Ozaki, T., Kawashima, R., 2004. A state-space model of the hemodynamic approach: nonlinear filtering of BOLD signals. *NeuroImage* 21, 547–567. doi:10.1016/j.neuroimage.2003.09.052.
- 620 Rolls, E.T., Cheng, W., Feng, J., 2021. Brain dynamics: Synchronous peaks, functional connectivity, and its temporal variability. *Human brain mapping* 42, 2790–2801. doi:10.1002/hbm.25404.
- Ruiz-Euler, H.C., Marques, J.R.F., Kappen, H.J., 2018. Nonlinear deconvolution by sampling biophysically plausible hemodynamic models. [arXiv:1803.08797](https://arxiv.org/abs/1803.08797).
- Schwarz, G., 1978. Estimating the dimension of a model. *The Annals of Statistics* 6, 461–464. doi:10.1214/aos/1176344136.
- 625 Setsompop, K., Gagoski, B.A., Polimeni, J.R., Witzel, T., Wedeen, V.J., Wald, L.L., 2011. Blipped-controlled aliasing in parallel imaging for simultaneous multislice echo planar imaging with reduced g-factor penalty. *Magnetic Resonance in Medicine* 67, 1210–1224. doi:10.1002/mrm.23097.
- Shmueli, K., van Gelderen, P., de Zwart, J.A., Horovitz, S.G., Fukunaga, M., Jansma, J.M., Duyn, J.H., 2007. Low-frequency fluctuations in the cardiac rate as a source of variance in the resting-state fMRI BOLD signal. *NeuroImage* 38, 306–320. doi:10.1016/j.neuroimage.2007.07.037.
- Sporns, O., Faskowitz, J., Teixeira, A.S., Cutts, S.A., Betzel, R.F., 2021. Dynamic expression of brain functional systems disclosed by fine-scale analysis of edge time series. *Network neuroscience* (Cambridge, Mass.) 5, 405–433. doi:10.1162/netn_a_00182.
- 630 Sreenivasan, K.R., Havlicek, M., Deshpande, G., 2015. Nonparametric hemodynamic deconvolution of fMRI using homomorphic filtering. *IEEE Transactions on Medical Imaging* 34, 1155–1163. doi:10.1109/tmi.2014.2379914.

- Tagliazucchi, E., Balenzuela, P., Fraiman, D., Chialvo, D.R., 2012. Criticality in large-scale brain fmri dynamics unveiled by a novel point process analysis. *Frontiers in physiology* 3, 15. doi:10.3389/fphys.2012.00015.
- 640 Tagliazucchi, E., Balenzuela, P., Fraiman, D., Montoya, P., Chialvo, D.R., 2011. Spontaneous bold event triggered averages for estimating functional connectivity at resting state. *Neuroscience letters* 488, 158–163. doi:10.1016/j.neulet.2010.11.020.
- 645 Tagliazucchi, E., Siniatchkin, M., Laufs, H., Chialvo, D.R., 2016. The voxel-wise functional connectome can be efficiently derived from co-activations in a sparse spatio-temporal point-process. *Frontiers in neuroscience* 10, 381. doi:10.3389/fnins.2016.00381.
- Tarun, A., Wainstein-Andriano, D., Sterpenich, V., Bayer, L., Perogamvros, L., Solms, M., Ax-macher, N., Schwartz, S., Ville, D.V.D., 2020. NREM sleep stages specifically alter dynamical integration of large-scale brain networks. *Iscience* 24, 101923. doi:10.1101/2020.07.08.193508.
- 650 Tibshirani, R., 1996. Regression shrinkage and selection via the lasso. *Journal of the Royal Statistical Society: Series B (Methodological)* 58, 267–288. doi:10.1111/j.2517-6161.1996.tb02080.x.
- Triantafyllou, C., Hoge, R., Krueger, G., Wiggins, C., Potthast, A., Wiggins, G., Wald, L., 2005. Comparison of physiological noise at 1.5 t, 3 t and 7 t and optimization of fMRI acquisition parameters. *NeuroImage* 26, 243–250. doi:10.1016/j.neuroimage.2005.01.007.
- 655 Uruñuela, E., Jones, S., Crawford, A., Shin, W., Oh, S., Lowe, M., Caballero-Gaudes, C., 2020. Stability-based sparse paradigm free mapping algorithm for deconvolution of functional MRI data. *Proceedings of the Annual International Conference of the IEEE Engineering in Medicine and Biology Society, EMBS 2020-July*, 1092–1095. doi:10.1109/embc44109.2020.9176137.
- Uruñuela-Tremiño, E., Moia, S., Gonzalez-Castillo, J., Caballero-Gaudes, C., 2019. Deconvolution of multi-echo functional MRI data with multivariate multi-echo sparse paradigm free mapping. *ISMRM 27th Annual Meeting and Exhibition*.
- Zhang, X., Pan, W.J., Keilholz, S.D., 2020. The relationship between BOLD and neural activity arises from temporally sparse events. *NeuroImage* 207, 116390. doi:10.1016/j.neuroimage.2019.116390.
- 660 Zöller, D., Sandini, C., Karahanoğlu, F.I., Padula, M.C., Schaer, M., Eliez, S., Ville, D.V.D., 2019. Large-scale brain network dynamics provide a measure of psychosis and anxiety in 22q11.2 deletion syndrome. *Biological Psychiatry: Cognitive Neuroscience and Neuroimaging* 4, 881–892. doi:10.1101/551796.

Supplementary Material for Hemodynamic Deconvolution Demystified: Sparsity-Driven Regularization at Work

670

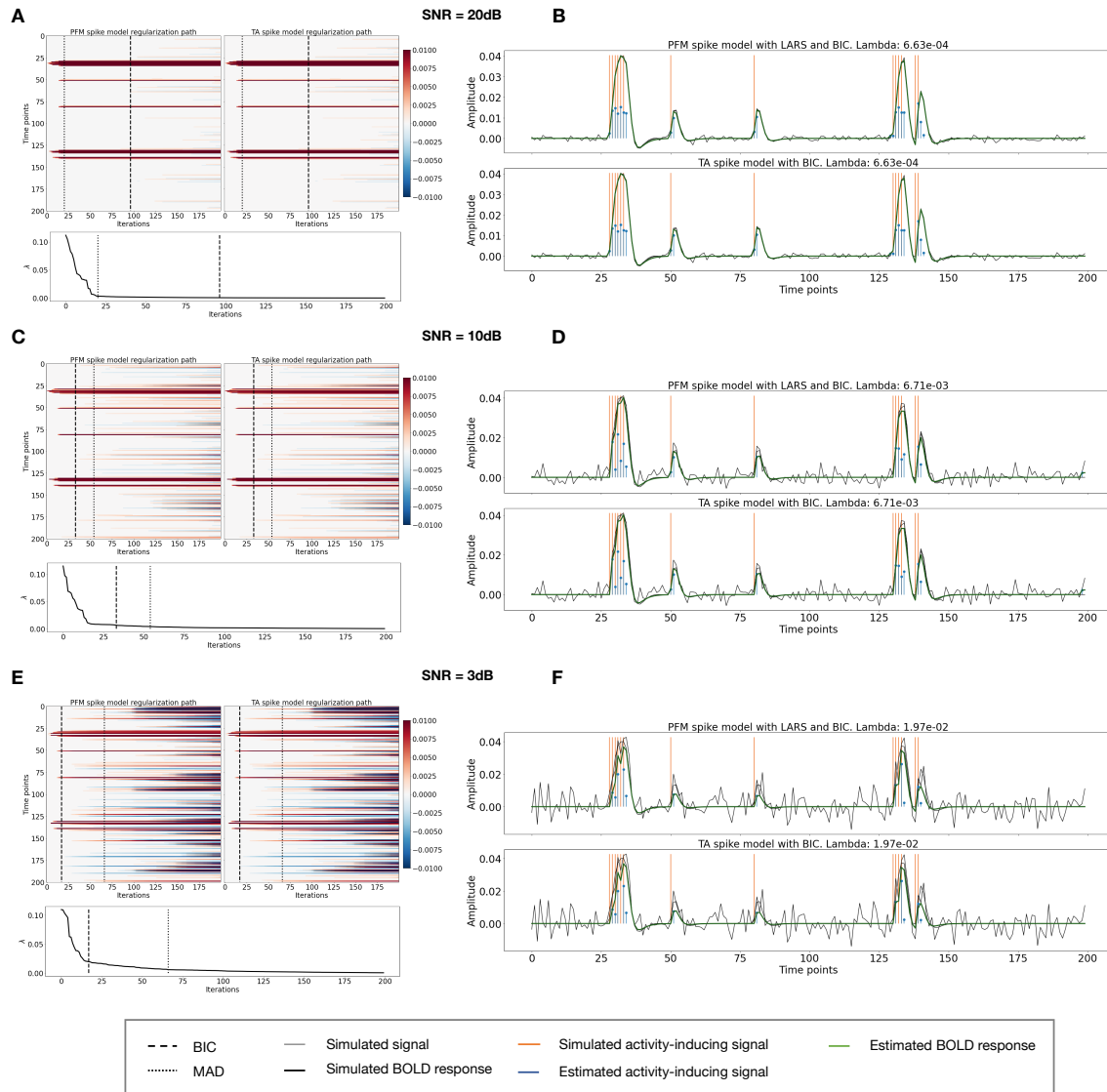


Figure S1: Spike model simulations. (Left) Heatmap of the regularization paths of the activity-inducing signal estimated with PFM and TA as a function of λ (increasing number of iterations in x-axis), whereas each row in the y-axis shows one time-point. Vertical lines denote iterations corresponding to the Akaike and Bayesian Information Criteria (AIC and BIC) optima. (Right) Estimated activity-inducing (blue) and activity-related (green) signals when set based on BIC. All estimates of are identical, regardless of SNR.

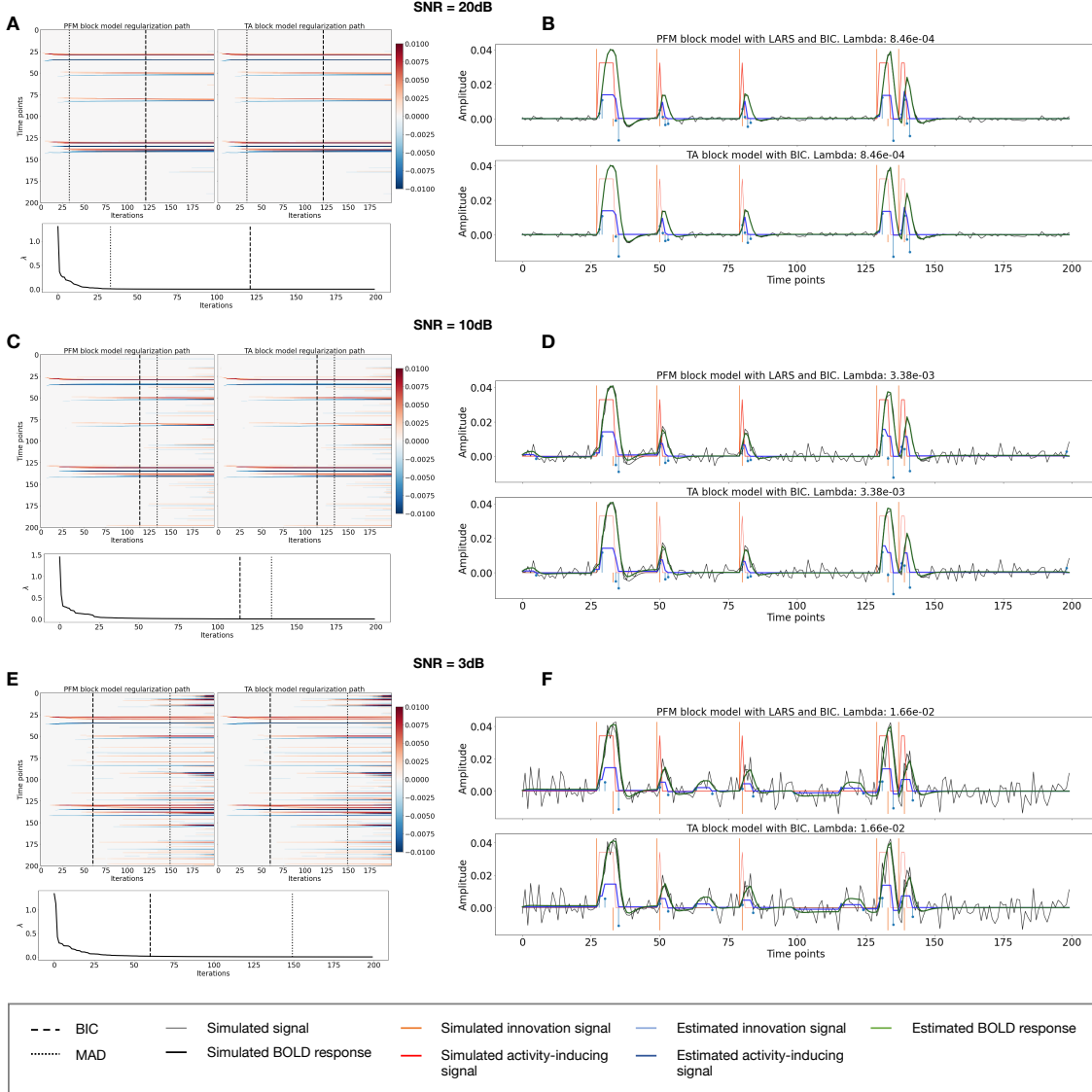


Figure S2: Block model simulations. (Left) Heatmap of the regularization paths of the innovation signal estimated with PFM and TA as a function of λ (increasing number of iterations in x-axis), whereas each row in the y-axis illustrates one time-point. Vertical lines denote iterations corresponding to the Akaike and Bayesian Information Criteria (AIC and BIC) optima. (Right) Estimated innovation (blue) and activity-related (green) signals when λ is set based on BIC. All the estimates are identical when compared between the PFM and TA cases, regardless of SNR.

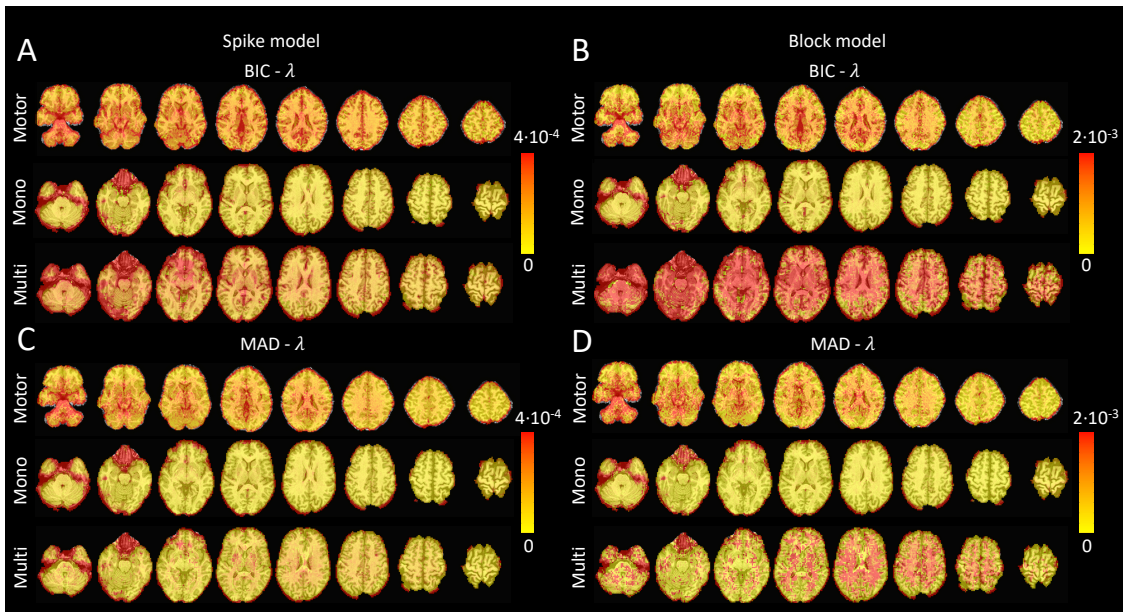


Figure S3: Values of λ across the different voxels in the brain used to estimate (A) the activity-inducing signal (spike model) and (B) the innovation signal (block model) with the BIC selection, as well as (C) the activity-inducing signal (block model) and (D) the innovation signal (block model) with a MAD-based selection. The λ maps are shown for the three experimental fMRI datasets: the motor task (Motor), the monoband resting-state (Mono), and the multiband resting-state (Multi) datasets.

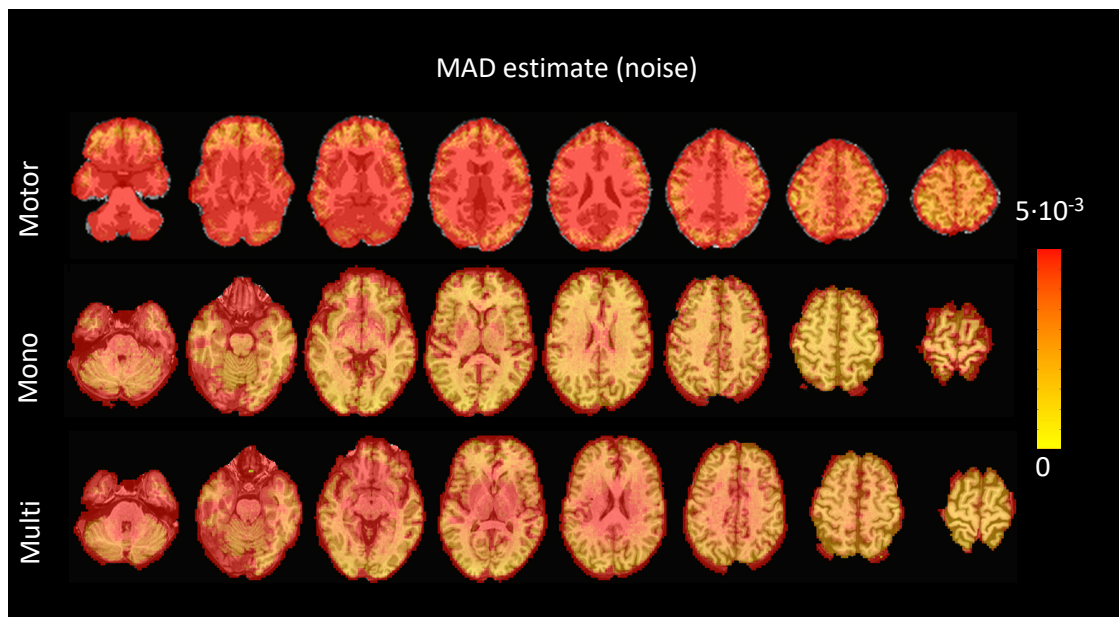


Figure S4: Values of the MAD estimate of standard deviation of the noise across the different voxels in the brain for the three experimental fMRI datasets: the motor task (Motor), the monoband resting-state (Mono), and the multiband resting-state (Multi) datasets.

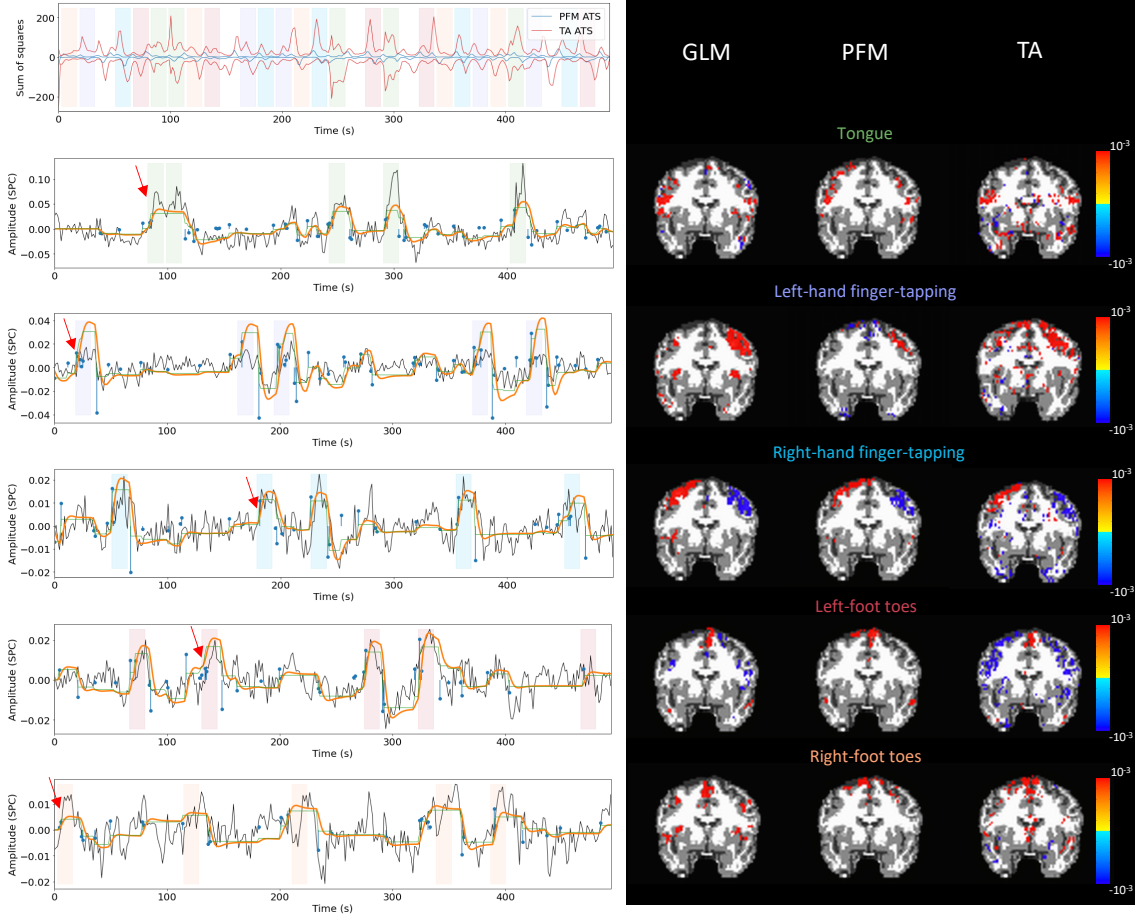


Figure S5: Activity maps of the motor task using a selection of λ based on the MAD estimate. Row 1: Activation time-series of the innovation signals estimated by PFM (in blue) or TA (in red) calculated as the sum of squares of all voxels at every timepoint. Positive-valued and negative-valued contributions were separated into two distinct time-courses. Color-bands indicate the onset and duration of each condition in the task (green: tongue, purple: left-hand finger-tapping, blue: right-hand finger-tapping, red: left-foot toes, orange: right-foot toes). Rows 2-6: time-series of a representative voxel for each task with the PFM-estimated innovation (blue), PFM-estimated activity-inducing (green), and activity-related (i.e., fitted, orange) signals, with their corresponding GLM, PFM, and TA maps on the right. The maps shown on the right are sampled at the time-point labeled with the red arrows and display the innovation signals at that moment across the whole brain.

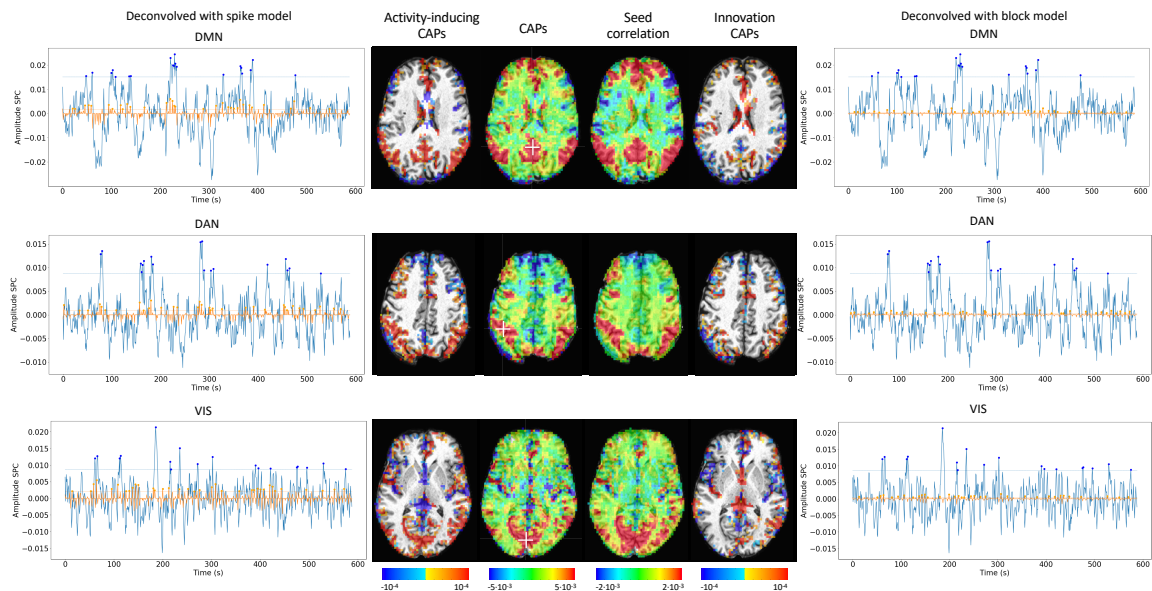


Figure S6: Activity-inducing CAPs (left) and innovation CAPs (right) obtained with the PFM-estimated activity-inducing and innovation signals respectively, using a MAD-based selection of λ . Time-points selected with a 95th percentile threshold are shown over the average time-series (blue) in the seed region (white-cross) and the deconvolved signal (orange). CAPs and seed correlation maps are illustrated in the center.